Article

Developmental Cell

Hedgehog signaling reprograms hair follicle niche fibroblasts to a hyper-activated state

Graphical abstract

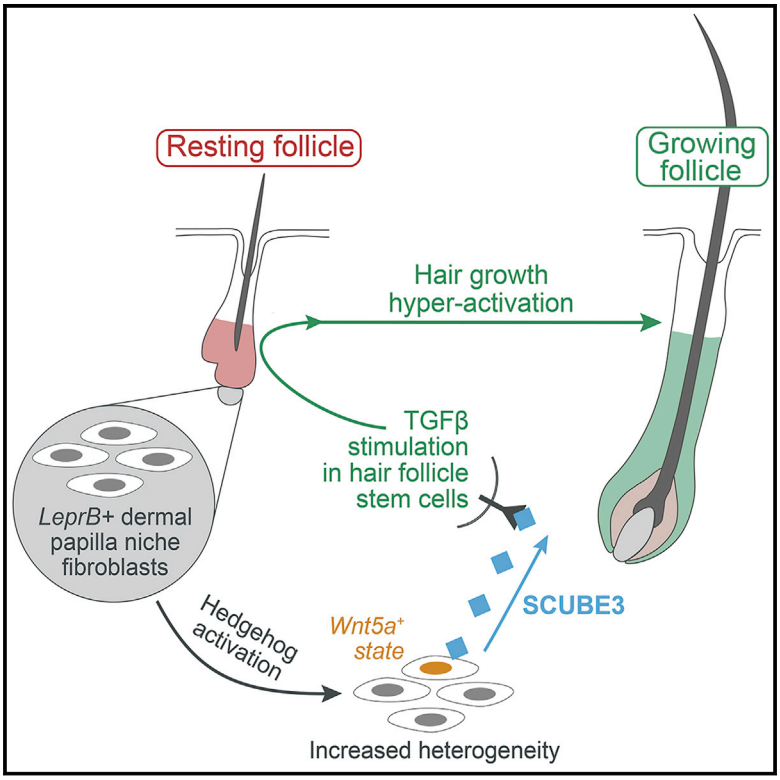

Authors

Yingzi Liu, Christian F. Guerrero-Juarez, Fei Xiao, ..., Qing Nie, Ji Li, Maksim V. Plikus

Correspondence

liji_xy@csu.edu.cn (J.L.), plikus@uci.edu (M.V.P.)

In brief

Liu and Guerrero-Juarez et al. demonstrate that genetic tools based on the leptin receptor gene *Lepr* can efficiently target hair follicle niche fibroblasts, called dermal papilla cells. Transgenic stimulation of the Hedgehog pathway in murine dermal papilla cells results in overactivation of hair growth via a downstream SCUBE3-TGF-β signaling mechanism.

Highlights

- Hedgehog signaling in murine fibroblasts induces new hair growth and hair multiplication
- Hedgehog activation increases fibroblast heterogeneity and drives new cell states
- TGF-β pathway downstream of dermal Hedgehog mediates hair growth hyper-activation
- SCUBE3 is a new mesenchymal niche factor that activates hair growth

Liu et al., 2022, Developmental Cell *57*, 1758–1775
July 25, 2022
https://doi.org/10.1016/j.devcel.2022.06.005

CellPress

CellPress

Developmental Cell

Article

Hedgehog signaling reprograms hair follicle niche fibroblasts to a hyper-activated state

Yingzi Liu,[1,2,3,20] Christian F. Guerrero-Juarez,[2,3,4,5,6,20] Fei Xiao,[2,3] Nitish Udupi Shettigar,[2,3,7] Raul Ramos,[2,3,5,6] Chen-Hsiang Kuan,[8,9] Yuh-Charn Lin,[10,11] Luis de Jesus Martinez Lomeli,[12] Jung Min Park,[13,14] Ji Won Oh,[13,14,15] Ruiqi Liu,[16] Sung-Jan Lin,[9,17] Marco Tartaglia,[18] Ruey-Bing Yang,[11] Zhengquan Yu,[16] Qing Nie,[2,4,5,6] Ji Li,[1,19,*] and Maksim V. Plikus[2,3,5,6,21,*]

[1]Department of Dermatology, Xiangya Hospital, Central South University, Changsha, Hunan 410008, China
[2]Department of Developmental and Cell Biology, University of California, Irvine, Irvine, CA 92697, USA
[3]Sue and Bill Gross Stem Cell Research Center, University of California, Irvine, Irvine, CA 92697, USA
[4]Department of Mathematics, University of California, Irvine, Irvine, CA 92697, USA
[5]Center for Complex Biological Systems, University of California, Irvine, Irvine, CA 92697, USA
[6]NSF-Simons Center for Multiscale Cell Fate Research, University of California, Irvine, Irvine, CA 92697, USA
[7]Amplifica Holdings Group, Inc., San Diego, CA 92128, USA
[8]Division of Plastic Surgery, Department of Surgery, National Taiwan University Hospital, Taipei, Taiwan
[9]Research Center for Developmental Biology and Regenerative Medicine, National Taiwan University, Taipei, Taiwan
[10]Department of Physiology, School of Medicine, College of Medicine, Taipei Medical University, Taipei, Taiwan
[11]Institute of Biomedical Sciences, Academia Sinica, Taipei, Taiwan
[12]Department of Statistics, University of California, Irvine, Irvine, CA 92697, USA
[13]Department of Anatomy, Yonsei University College of Medicine, Seoul, Korea
[14]Department of Anatomy, School of Medicine, Kyungpook National University, Daegu, Korea
[15]Hair Transplantation Center, Kyungpook National University Hospital, Daegu, Korea
[16]State Key Laboratories for Agrobiotechnology, College of Biological Sciences, China Agricultural University, Beijing 100193, China
[17]Institute of Biomedical Engineering and Department of Dermatology, National Taiwan University, Taipei, Taiwan
[18]Genetics and Rare Diseases Research Division, Ospedale Pediatrico Bambino Gesù, IRCCS, Rome 00146, Italy
[19]Hunan Key Laboratory of Aging Biology, Xiangya Hospital, Central South University, Changsha, Hunan 410008, China
[20]These authors contributed equally
[21]Lead contact
*Correspondence: liji_xy@csu.edu.cn (J.L.), plikus@uci.edu (M.V.P.)
https://doi.org/10.1016/j.devcel.2022.06.005

SUMMARY

Hair follicle stem cells are regulated by dermal papilla fibroblasts, their principal signaling niche. Overactivation of Hedgehog signaling in the niche dramatically accelerates hair growth and induces follicle multiplication in mice. On single-cell RNA sequencing, dermal papilla fibroblasts increase heterogeneity to include new *Wnt5a*^{high} states. Transcriptionally, mutant fibroblasts activate regulatory networks for Gli1, Alx3, Ebf1, Hoxc8, Sox18, and Zfp239. These networks jointly upregulate secreted factors for multiple hair morphogenesis and hair-growth-related pathways. Among these is non-conventional TGF-β ligand *Scube3*. We show that in normal mouse skin, *Scube3* is expressed only in dermal papillae of growing, but not in resting follicles. SCUBE3 protein microinjection is sufficient to induce new hair growth, and pharmacological TGF-β inhibition rescues mutant hair hyper-activation phenotype. Moreover, dermal-papilla-enriched expression of *SCUBE3* and its growth-activating effect are partially conserved in human scalp hair follicles. Thus, Hedgehog regulates mesenchymal niche function in the hair follicle via SCUBE3/TGF-β mechanism.

INTRODUCTION

In recent years, the field of fibroblast biology has experienced a significant progress, largely due to the coming-of-age of single-cell profiling technologies (LeBleu and Neilson, 2020; Lynch and Watt, 2018). Fibroblasts in the stroma of different organs have long been regarded to be far more functionally diverse than what can be assumed from their stereotypical spindle-like appearance in culture and shared marker genes, dominated by collagens and other extracellular matrix proteins (Plikus et al., 2021). Skin is particularly rich in fibroblasts, where they occupy several distinct locations within its dermal layer (Lynch and

Watt, 2018). Morphologically, dermis consists of (1) papillary layer, which contacts the epidermis; (2) reticular layer, which endows skin with most of its mechanical properties; and (3) dermal white adipose layer, which contains lipid-laden adipocytes and their fibroblast-like progenitors. Recent single-cell RNA sequencing (scRNA-seq) studies have revealed substantial transcriptional heterogeneity among skin fibroblasts (Abbasi et al., 2020; Gay et al., 2020; Guerrero-Juarez et al., 2019; Gupta et al., 2019; Lim et al., 2018; Mok et al., 2019; Philippeos et al., 2018; Shin et al., 2020; Tabib et al., 2018), whereas lineage tracing studies uncovered their genealogy during embryonic development and phenotypic plasticity in response to wounding (Correa-Gallegos et al., 2019; Driskell et al., 2013; Plikus et al., 2017; Rinkevich et al., 2015; Shook et al., 2020, 2018).

Skin also contains specialized fibroblasts of dermal papilla (DP) and dermal sheath (DS) that constitute the principal signaling niche of hair follicles (HFs) (Driskell et al., 2011; Morgan, 2014; Sennett and Rendl, 2012). The latter are periodically cycling mini organs that regenerate new hairs via the coordinated proliferation and differentiation of their epithelial cells. DP fibroblasts form discrete clusters at the base of each HF, where they regulate growth activities of the epithelial lineage. During the rest phase of the hair-growth cycle (*aka* telogen), DP cells come in contact with the so-called secondary hair germ (HG) cells, which are the progenies of the *bona fide* bulge stem cells (SCs). Signals from telogen DP cells help to maintain HG and bulge SCs in a prolonged quiescence (Greco et al., 2009; Oshimori and Fuchs, 2012). Change in the DP signaling output heralds the initiation of the growth phase of the cycle (*aka* anagen) (Botchkarev et al., 2001; Enshell-Seijffers et al., 2010a; Greco et al., 2009; Harel et al., 2015; Hawkshaw et al., 2020; Legrand et al., 2016; Oshimori and Fuchs, 2012; Telerman et al., 2017). Activated HFs undergo rapid epithelial lineage expansion, wherein epithelial progenitors give rise to the so-called hair matrix cells, whose proliferation sustains hair growth. Surrounded by the hair matrix during anagen, DP repositions away from the bulge and deep into dermal adipose layer. There, activated DP fibroblasts send essential instructive cues to sustain hair-making activities by matrix cells (Chi et al., 2013; Clavel et al., 2012; Enshell-Seijffers et al., 2010a; Rompolas et al., 2012) and pigment producing activities by melanocytes (Enshell-Seijffers et al., 2010b). DP is also connected to DS, which during anagen "encases" the entire length of the cylindrically shaped HF and houses a distinct population of cells that serve as progenitors for DP fibroblasts (González et al., 2017; Hagner et al., 2020; Heitman et al., 2020; Rahmani et al., 2014; Shin et al., 2020). Growth activities by anagen HF cease after a period of time, at which point most of its epithelial lineage undergoes apoptosis-driven involution (*aka* catagen). Bulge SC progeny in the upper part of the anagen HF cylinder, called outer root sheath, survive catagen and reorganize into new HG during the consecutive telogen (Hsu et al., 2011). The sheath-like DS undergoes active contraction (Heitman et al., 2020), which assists with catagen HF remodeling and actively repositions DP upward next to the HG.

During skin development, DP and DS fibroblasts progressively specify from the dermal condensate progenitors that form at the interface with the embryonic epidermis as part of the HF morphogenesis program (Biggs et al., 2018; Sennett et al., 2015). Recent scRNA-seq studies on embryonic mouse skin have defined the progressive specification stages of dermal condensate progenitors, their heterogeneity, and associated gene expression programs (Ge et al., 2020; Gupta et al., 2019; Mok et al., 2019). Normally, DP and DS fibroblasts do not form *de novo* in the adult skin because the HF morphogenesis program becomes inaccessible. However, it can be re-activated in the center of large excisional wounds, where many new HFs with new DP and DS cells regenerate (Ito et al., 2007). Lineage studies indicate that the latter form *de novo* from originally non-hair fated wound myofibroblasts (Abbasi et al., 2020; Lim et al., 2018; Plikus et al., 2017). Although the epigenetic basis of wounding-induced myofibroblast plasticity are not well understood, the process requires canonical WNT (Ito et al., 2007), retinoic acid (Abbasi et al., 2020; Kim et al., 2019), and Hedgehog signaling events (Lim et al., 2018).

Lineage-specific genetic tools are necessary to precisely study HF fibroblasts; however, their repertoire remains limited. Embryonic dermal condensate progenitors can be targeted with *Tbx18-Cre* (Clavel et al., 2012), whereas adult DS fibroblasts, with *Sma-CreER^{T2}* (Rahmani et al., 2014) and *Acan-CreER* (Heitman et al., 2020). DP fibroblasts activate *Sox18-CreER^{T2}* at birth (Legrand et al., 2016), *Corin-Cre* soon after birth (Enshell-Seijffers et al., 2010a), and *CD133-CreER^{T2}* in adult skin, albeit only with low efficiency (Zhou et al., 2016). Here, we confirm that in mouse skin, Leptin receptor (*Lepr*) is a faithful DP marker gene (Greco et al., 2009; Rezza et al., 2016) and show that isoform B-specific *LeprB-Cre* (DeFalco et al., 2001) and *LeprB-CreER* can be used to efficiently target postnatal DP fibroblasts. Using these genetic tools, we uncover how DP fibroblast lineage and signaling niche are regulated by the Hedgehog pathway. We show that cell-autonomous activation of Hedgehog increases DP fibroblast heterogeneity and produces distinct hyper-activated DP states, characterized by unique regulatory networks and multi-pathway secretome. These distinct DP states, in turn, induce hair-growth hyper-activation and embryonic-like formation of neogenic HFs, a morphogenetic program, typically inaccessible in adult skin.

RESULTS

Lepr marks hair follicle mesenchyme

To identify genetic tools for targeting DP fibroblasts, we re-examined bulk-level and single-cell transcriptomic datasets for mouse HF cells. *Lepr* has been identified as a DP signature gene (Greco et al., 2009; Rezza et al., 2016) (Figure 1A). Analysis of protein-coding alternatively spliced isoforms (Gorska et al., 2010) suggests that DP fibroblasts are dominated by the *Lepr-203* transcript (78% on average), which codes for the 894-amino acid-long isoform A of the LEPR protein (Figure 1A). Only 3% of *Lepr* transcripts are of the *Lepr-201* isoform, which code for the 1,162-amino acid-long isoform B. We also examined *Lepr* expression in scRNA-seq datasets from postnatal week 5 (anagen) and week 9 (telogen) mouse skin (Joost et al., 2020). *Lepr* is specifically expressed in both anagen and telogen DP fibroblasts and to a lesser extent by DS fibroblasts, with no expression in keratinocytes or other skin cell types (Figure 1B).

Next, we profiled *Lepr* expression in postnatal mouse skin by RNAscope (n = 3 mice per time point) using a pan-isoform *Lepr*

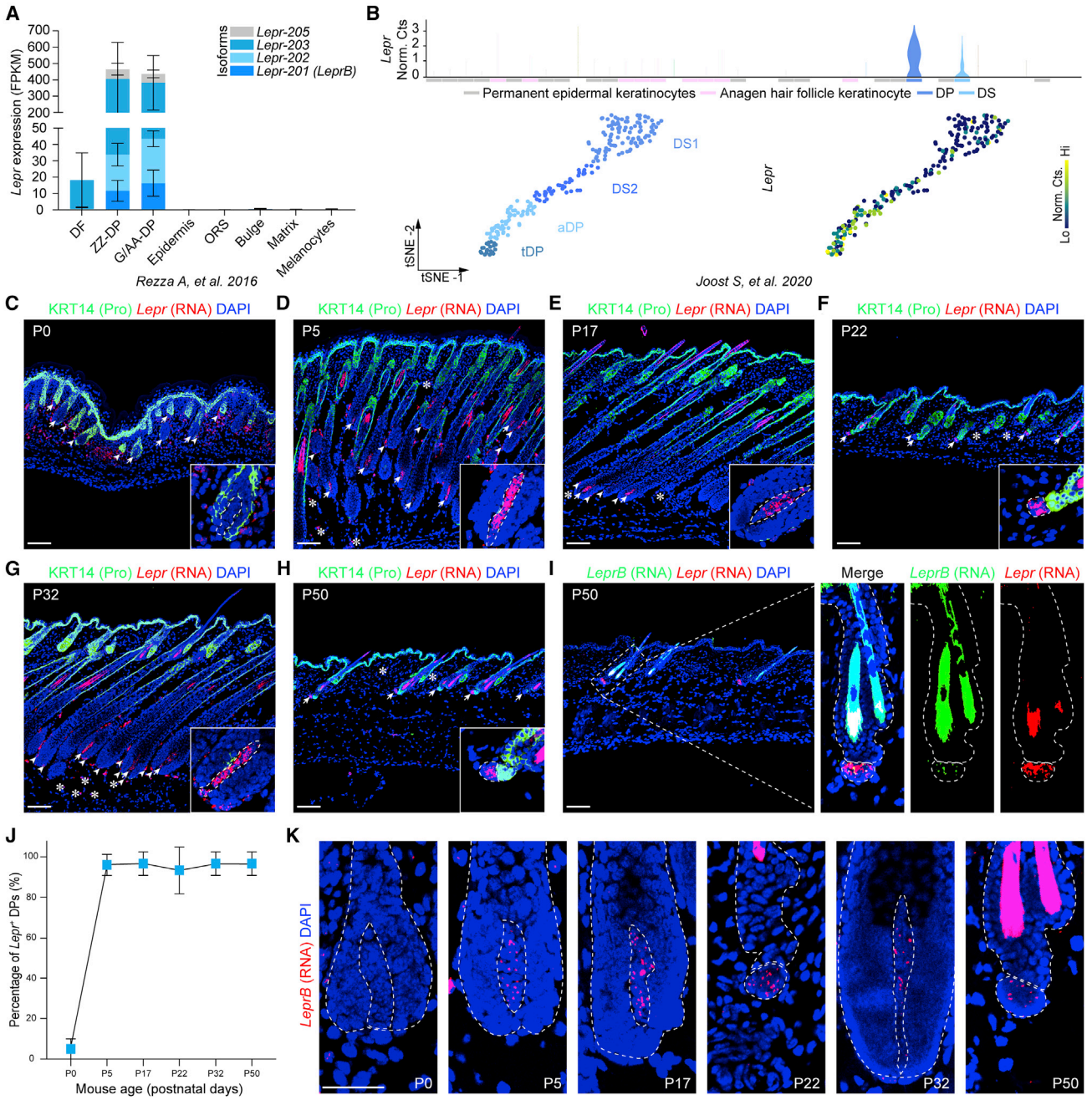

Figure 1. *Lepr* is a marker gene of hair follicle mesenchyme

(A) In P5 mouse skin RNA-seq data, *Lepr* is highly enriched in DP fibroblasts. Relative proportions of four *Lepr* transcripts are shown.

(B) Violin plots (top) for *Lepr* in combined week 5 (anagen) and week 9 (telogen) mouse skin scRNA-seq data (Joost et al., 2020). tSNE plots show DP and DS identities (bottom left) and *Lepr* expression distribution (bottom right).

(C–H) Co-expression of pan-isoform *Lepr* mRNA (red) and KRT14 (green) in dorsal mouse skin. *Lepr* expression sites are marked as follows: DP (arrows), peri-follicular dermal cells (arrowheads), dermal adipose, and dermis (asterisks). Inserts show magnified DPs.

(I) Pan-isoform *Lepr* (red) and isoform-specific *LeprB* (green) co-localize in DPs at P50.

(J) Quantification of *Lepr*$^{+}$ DPs at indicated postnatal time points.

(K) Isoform-specific *LeprB* (red) shows high DP specificity. Tissue sections were counterstained with DAPI in (C–I and K).

Abbreviations: DF, dermal fibroblasts; ZZ-DP, zigzag DP fibroblasts; G/AA-DP, guard, awl, and auchene DP fibroblasts; ORS, outer root sheath; aDP, anagen DP; tDP, telogen DP; DS, dermal sheath; and Norm. Cts., normalized counts. Scale bars, 100 μm in (C–I) and 50 μm in (K).

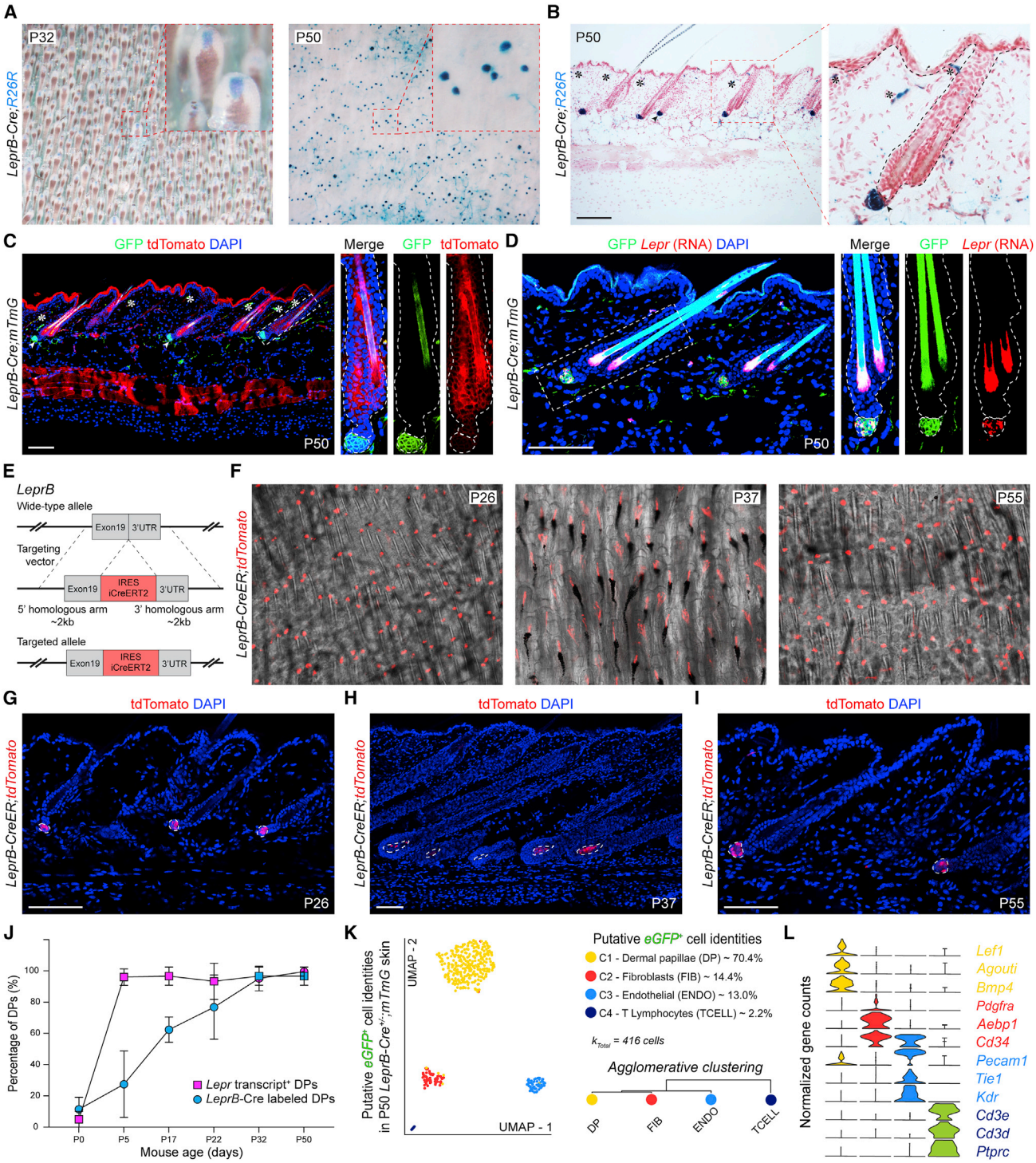

Figure 2. *LeprB-Cre* efficiently targets dermal papillae

(A and B) Whole mount (A) and histology (B) showing β-galactosidase activity patterns (blue) in *LeprB-Cre;R26R* skin. Note: β-galactosidase activity in DPs, peri-follicular cells (arrowheads), dermal adipose, and vessel-like structures (asterisks).

(C) GFP (green) and tdTomato (red) reporter patterns in *LeprB-Cre;mTmG* skin at P50. GFP is prominent in DPs and also shows in rare peri-follicular cells (arrowheads), dermal adipose, and in scattered cells in the upper dermis (asterisks).

(D) Co-expression patterns of pan-isoform *Lepr* mRNA (red) and GFP reporter (green) in *LeprB-Cre;mTmG* skin at P50.

(E) Schematic diagram of *LeprB-CreER* transgenic mouse generation.

(legend continued on next page)

probe. At postnatal day 0 (P0), *Lepr* expression was localized to the developing dermal adipose layer, including the peri-follicular region (Figure 1C, arrowheads), with DPs being largely devoid of transcript (Figure 1C, arrows). This expression pattern was dramatically altered by P5, when most of *Lepr* transcript localized to DPs of early stage anagen HFs (Figure 1D, arrows). Scattered expression was observed in the peri-follicular (Figure 1D, arrowheads) and expanded dermal adipose layer (Figure 1D, asterisks). This expression pattern is consistent with the P5 RNA-seq data from Rezza et al. (2016), and it remained largely preserved in late first anagen at P17 (Figure 1E) and then repeated during second anagen at P32 (Figure 1G). During first and second telogen phases at P22 and P50, respectively, *Lepr* remained strongly expressed in DPs (Figures 1F and 1H, arrows) with only scattered positive cells found outside of HFs (Figures 1F and 1H, asterisks). The majority of HFs contained *Lepr*$^{+}$ DPs by P5, plateauing and remaining consistent throughout P50 (Figure 1J). DP specificity was also maintained when probing for *LeprB* isoform transcript (Figure 1I, green; 1K, red). Lower expression levels seen with *LeprB*-specific probe compared with pan-isoform probe are consistent with *LeprB* being only a minor fraction of the protein-coding *Lepr* transcripts in P5 DPs on RNA-seq (Rezza et al., 2016) (Figure 1A). Thus, *Lepr* is a DP marker gene with a hair cycle-independent expression pattern.

LeprB-Cre targets dermal papilla fibroblasts

We then asked if *Lepr*-based genetic tools can be used to achieve efficient DP fibroblast targeting. We examined the previously reported *LeprB-Cre* mouse line, where an *IRES-Cre* recombinase expression cassette is placed into the 3′ untranslated region of *Lepr*, allowing for *Cre* activity to be restricted to cells transcribing *LeprB* isoform (DeFalco et al., 2001) (Figure S1A). We characterized labeling pattern in dorsal skin of *LeprB-Cre;R26R* and *LeprB-Cre;mTmG* reporter mice. We observed labeling in three skin compartments: (1) dermal adipose layer, (2) papillary dermis, and (3) DPs. Labeling in the developing dermal adipose layer, including around developing HFs, was evident as early as P0 (Figures S1D and S1F, arrowheads) and became prominent at P3 (Figures S1B and S1D). At later time points, adipose labeling became more restricted (Figures 2A, 2B, and S1C–S1J), with only 18.2% and 24.2% of perilipin (PLIN)-expressing mature adipocytes being GFP reporter-positive in P32 and P50 *LeprB-Cre;mTmG* skin (n = 3 mice per time point), respectively (Figures S1L–S1N). At P32, most of the PLIN^{+}/GFP^{+} adipocytes localized within the upper adipose layer, along the length of anagen HFs, and only 0.5% of adipocytes located below HFs were PLIN^{+}/GFP^{+} (Figures S1L and S1N). Scattered reporter-positive adipose layer cells localized in close proximity to the HFs (Figures 2C, S1J, and S1K, arrowheads). In papillary dermis, only rare micro-vessel-like structures were reporter-positive as early as P3 and their abundance remained low at all time points analyzed (Figures 2A–2C and S1D–S1J, asterisks). In DPs, first scattered reporter-positive cells were observed at P0 (Figure S1D) and continued to be rare at P3 (Figures S1B and S1D), P5 (Figure S1G), and P7 (Figure S1D). DP labeling progressively increased by late first anagen (Figures S1D and S1H), became high yet incomplete during first telogen (Figures S1C, S1E, and S1I) and second anagen (Figures 2A, S1E, and S1J) at P22 and P32, respectively, and eventually became high and nearly complete by second telogen at P50 (Figures 2A–2D and S1K). Quantification of reporter-positive DPs supports progressively increasing labeling during early postnatal phases with almost complete labeling by P50 (Figure 2J). RNAscope further confirmed expression of pan-isoform *Lepr* and isoform-specific *LeprB* in GFP^{+} DP fibroblasts in P50 *LeprB-Cre;mTmG* skin (Figures 2D and S1K). We also performed scRNA-seq on GFP^{+} cells sorted from dorsal skin of *LeprB-Cre;mTmG* mice at P50, which helped to fully resolve the identify of *LeprB-Cre* marked cells and further confirmed efficient DP targeting (Figures 2K, 2L, and S2).

To enable inducible labeling and targeting of DPs based on their expression of *LeprB* isoform, we generated new *LeprB-CreER* transgenic mice in which *IRES-iCreERT2* construct was inserted after exon 19 stop codon of the *Lepr* gene (Figure 2E). To test its specificity and efficacy, we treated *LeprB-CreER;tdTomato* mice with five daily doses of tamoxifen at three time points (n = 3 per time point): P21 (first telogen), P32 (second anagen), and P50 (second telogen). When skin was examined at day 6 post-induction, *LeprB-CreER* labeled DPs prominently and specifically at all three time points, with virtually no targeting of extra-follicular cells (Figures 2F–2I). Thus, we conclude that in dorsal mouse skin, constitutive *LeprB-Cre* most efficiently targets DPs, with labeling prominently increasing during the second hair-growth cycle, and that inducible *LeprB-CreER* can permit specific and efficient DP targeting both in telogen and anagen phases. We also note that the rest of the experiments described below were performed using *LeprB-Cre*.

Dermal Hedgehog activates hair growth

We asked if inducing constitutive Hedgehog signaling in dermal cells using *LeprB-Cre* can affect hair growth. Normally, Hedgehog is required for embryonic hair development (Chiang et al., 1999; St-Jacques et al., 1998; Woo et al., 2012) and for proper hair-growth activation (Paladini et al., 2005; Sato et al., 1999). We generated *LeprB-Cre;SmoM2*$^{+/-}$ mutant mice with constitutively active *Smoothened (SmoM2)* and compared their hair phenotypes with those of *LeprB-Cre* control mice. Hair growth was traced non-invasively via periodic hair clipping and photography as previously described (Plikus et al., 2008; Wang et al., 2017). Consistent with a relatively late onset of *LeprB-Cre* activation in DP fibroblasts (Figure 2J), mutant mice did not show obvious hair-growth cycle difference until second telogen. However, although no hair growth was observed in control mice (n = 8) during the entire observation period spanning second telogen days P46 through P86, mutant mice (n = 8) showed prominently

(F–I) Whole mount (F) and histology (G–I) showing tdTomato (red) expression in *LeprB-CreER;tdTomato* skin.
(J) Quantification of *LeprB-Cre*$^{+}$ DPs in *LeprB-Cre;mTmG* mice (based on GFP) and pan-isoform *Lepr*$^{+}$ DPs (from Figure 1J).
(K) UMAP visualization of unsupervised hierarchical clustering of all GFP^{+} cells from P50 *LeprB-Cre;mTmG* skin. Clusters are defined.
(L) Violin plots showing expression of selected marker genes. Tissue sections were counterstained with nuclear fast red in (B) and with DAPI in (C, D, and G–I). Scale bars, 100 μm in (B–D and G–I).

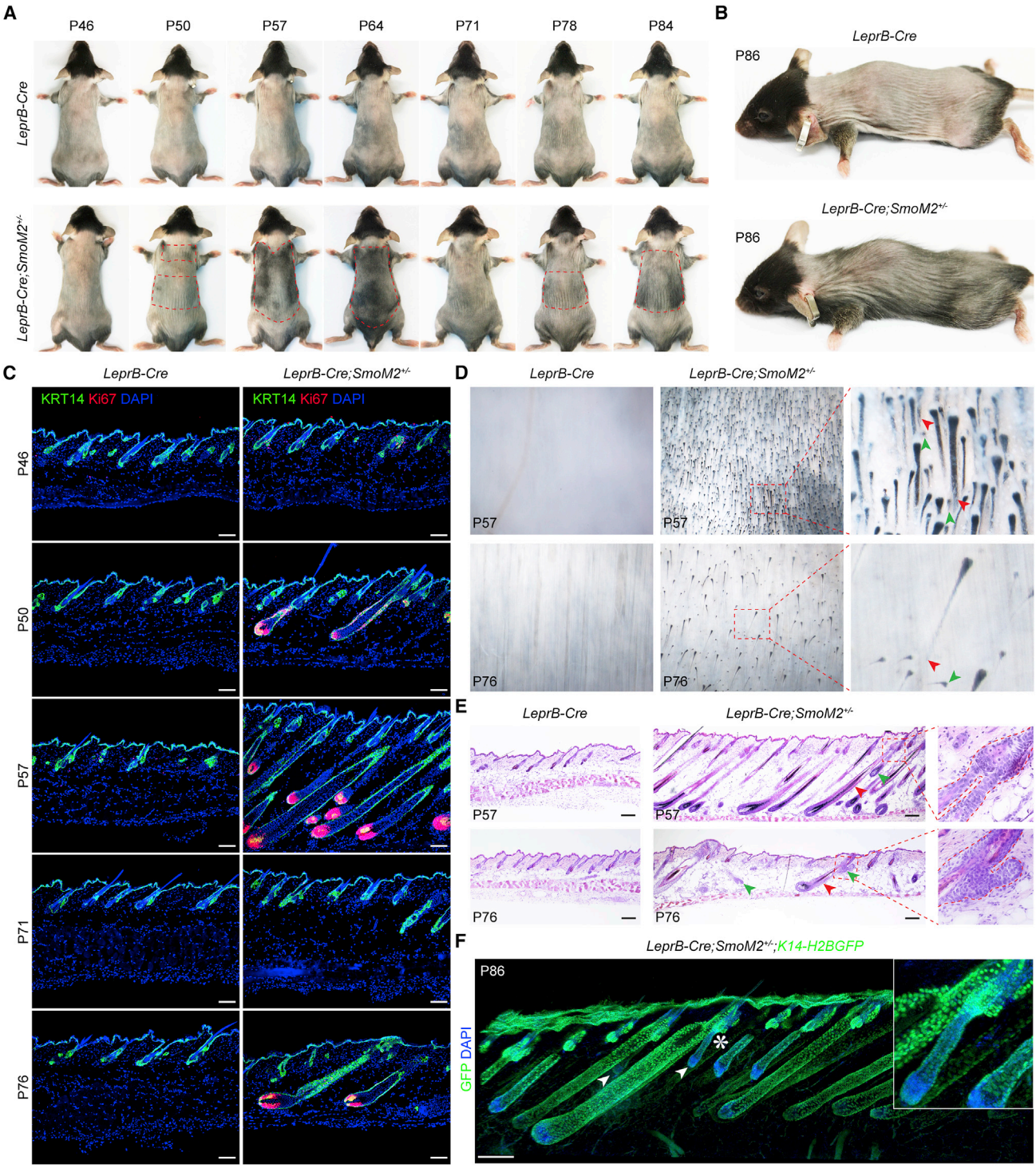

Figure 3. Hyper-activated hair regeneration in mice with dermal Hedgehog activation

(A) Time course analysis of dorsal hair-growth patterns in representative *LeprB-Cre;SmoM2*$^{+/-}$ mutant (bottom) and *LeprB-Cre* control mice (top) between days P46 and P84. Hair growth (dark regions, marked) is seen only in the mutant mouse.

(B) Representative images of mutant (bottom) and control mice (top) at P86. Diffuse hair growth is seen only in the mutant mouse.

(C) Co-expression of KRT14 (green) and Ki67 (red) in mutant (right) and control skin (left). Many anagen HFs with Ki67^{+} hair matrix are seen in mutant skin at P50, P57, and P76.

(legend continued on next page)

precocious hair growth (Figures 3A and S3A). Strikingly, hairs in mutant mice grew sparsely across the skin (Figure 3B), contrasting normal hair growth in adult wild-type mice, which occurs in coordinated waves as a result of HFs entering anagen collectively (Plikus et al., 2008; Wang et al., 2017). This was confirmed on whole mount at P57 and P76 (Figure 3D). Although at both time points, control HFs were in telogen, mutant skin contained numerous but sparsely patterned anagen HFs. This patterning feature was especially prominent at P76 (Figure 3D, bottom). Precocious anagen and general loss of normal hair-growth coordination was confirmed on histology and manifested starting at P50 (Figures 3C, 3E, and S3B). Importantly, in addition to precociously growing pre-existing HFs, mutant mice showed signs of HF multiplication, when small HFs were found growing physically connected to larger HFs at the SC region. Such neogenic HFs often grew at abnormal angles that did not follow normal cranio-caudal direction of pre-existing HFs (Figures 3E and 3F, arrowheads; Videos S1 and S2). Previously, analogous HF multiplication in adult mice has been observed upon epithelial activation of β-Catenin (Gat et al., 1998; Lo Celso et al., 2004) and, most recently, upon concomitant epidermal and dermal, but not dermal only, *Ptch1* deletion (Sun et al., 2020). These results suggest that *LeprB-Cre* enables efficient gene targeting to DP fibroblasts for studying the role of mesenchymal niche in hair growth and follicle neogenesis.

Hedgehog drives mesenchymal heterogeneity

To identify candidate cell types and molecular events that drive enhanced hair-growth downstream of Hedgehog activation, we profiled dorsal skin of *LeprB-Cre;SmoM2*$^{+/-}$*;mTmG* mutant and *LeprB-Cre;mTmG* control mice by scRNA-seq at P46 (Figure 4A), a time point that precedes the appearance of mutant hair phenotype by a few days (Figures 3C and S3B). Histological analysis confirmed telogen morphology of HFs in all sequenced mouse skin samples (Figures S4A and S4B). We reasoned that any single-cell transcriptome changes at this early time point would be more readily interpreted as the cause rather that the consequence of the mutant mouse phenotype. On data analysis (Figures 4B and 4C), prominent enrichment for mutant cells were observed among fibroblasts, which further sub-divided into seven DP, two DS, one fibro-adipogenic (FA) and twelve dermal fibroblast clusters (Figures 4D and 4F). DP clusters VI and VII were almost entirely composed of mutant cells that displayed dermal papilla-like gene expression (Figure 4E, left) and were collectively defined as DP-like (DPL) fibroblasts—DPL I and DPL II, respectively. A cluster of fibroblasts with dual adipogenic and contractile gene signature (Figure 4E, right) was also almost entirely made of mutant cells, which we defined as FA fibroblasts (FA-FIBs). Expression of *eGFP*, which serves as readout for Cre-lox recombination, was prominent in control and mutant DP clusters, and in mutant DPL and FA-FIB clusters (Figure 4G, left). However, expression of *eYFP* reporter, which is part of *SmoM2* fusion gene (Figure 4G, center), and high aggregate Hedgehog signaling score (Figure 4G, right) were nearly exclusive to mutant DPL and FA-FIB clusters. Both of these were mostly absent in other mutant fibroblasts, including non-DPL *eGFP*$^{+}$ DP clusters. This suggests that upon acquisition of *SmoM2* mutation, DP cells transition toward a DPL state. RNA velocity predicted consistent trajectories among DP clusters that start at cluster DP II; move across clusters DP I, III, and V; and end at DP IV (Figure S4F). Intriguingly, no DP-to-DPL trajectory was observed likely because DPL cells have already formed before our analysis at P46 (Figure S4F). However, DPL fibroblasts, marked by high *Wnt5a* expression, localized to the DP compartment when probed on RNAscope, supporting the notion that they convert from mutated DP cells *in situ* (Figures 4H and S4C, top). FA-FIBs, which co-express *Pcsk5* and *Lepr*, were present within dermal adipose layer, including near HFs (Figure 4H, bottom; Figures S4C and S4E). Together, the above data suggest that ectopic Hedgehog activation in *LeprB-Cre*$^{+}$ fibroblasts drives them to acquire transcriptionally distinct states and that *LeprB-Cre;SmoM2*$^{+/-}$ hair phenotypes are likely driven by newly formed, Hedgehog-active DPL fibroblasts.

Hedgehog-regulated hair follicle signaling

Next, we performed differential gene expression analysis comparing mutant DP (including DPL) versus control DP clusters using DESeq2 (Table S1). This analysis revealed prominent changes in DPL cells across transcription factor, extracellular matrix, and contractile gene categories and suggested that they become transcriptionally more similar to fibroblasts engaged in HF morphogenesis, either during embryogenic development or upon wound induced neogenesis (Figure S5).

We then studied signaling changes in telogen HFs using CellChat method (Jin et al., 2021). Analysis was performed jointly on DP/DPL fibroblasts, bulge SCs, and secondary HG cells, identifying 27 significantly activated signaling pathways between mutant versus control HF cells (Figure S6A). Several signaling pathways previously implicated in regulation of hair growth were prominently changed (Figure 5A) or became activated (Figure S6B) among mutant HF cells. These changes were largely driven by mutant DPL II fibroblasts (Figure 5B). BMP, TGF-β, and non-canonical WNT were examples of prominently "rewired" pathways in mutant HFs. A change in BMP pathway structure was driven by DPL II cells becoming a novel source of *Bmp4* and *Bmp7* ligands for autocrine signaling among DP fibroblasts (Figures 6A and S6E; Table S1). However, BMP signaling strength from mutant DP fibroblasts to bulge SCs/HG cells remained similar, attributed to lower expression of *Bmpr2* and *Acvr2a* receptors by the latter (Figures S6C–S6E). A change was identified in the TGF-β pathway, driven by DPL II cells becoming new cellular source for a non-classical activating

(D) Whole-mount view of control (left) and mutant skin (right) at P57 and P76. Many asynchronously cycling pigmented anagen HFs are seen only in mutant skin. Many small anagen HFs (green arrowheads) that often grow at abnormal angles relative to adjacent large anagen HFs (red arrowheads) can be seen in mutant skin.

(E) Histology of control (left) and mutant skin (right). Double HFs, consisting of a large, likely pre-existing HF (red arrowhead) and a small, likely neogenic HF (green arrowhead), are found throughout mutant skin.

(F) Reconstruction of dorsal skin in *LeprB-Cre;SmoM2*$^{+/-}$*;K14-H2BGFP* mouse at P86 after tissue clearing demonstrates neogenic HFs (arrowheads). Representative neogenic HF (asterisk) is magnified. Tissues were counterstained with DAPI in (C and F). Scale bars, 100 μm in (C, E, and F).

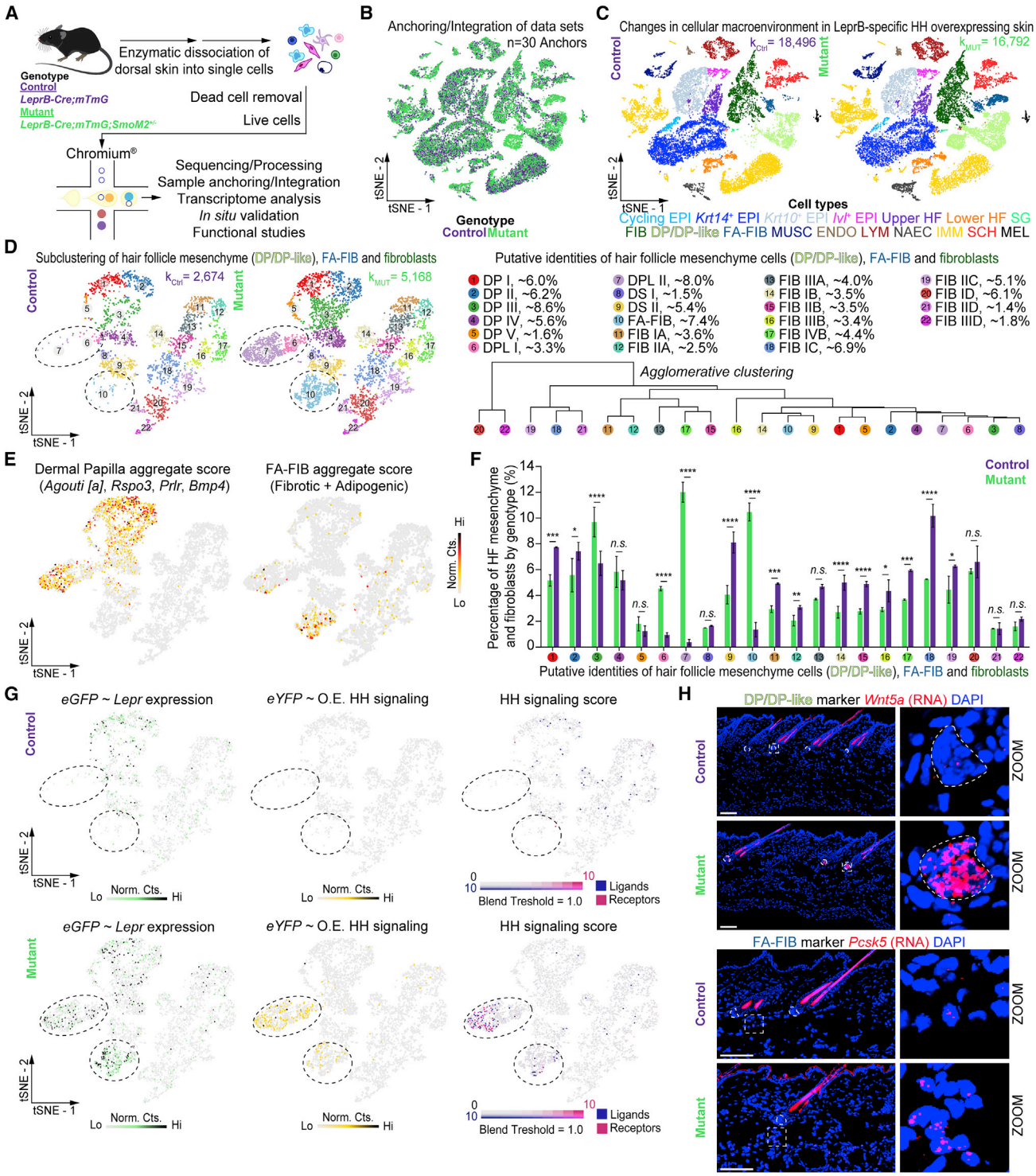

Figure 4. New fibroblast states form in response to Hedgehog activation

(A) Workflow of scRNA-seq experiment.

(B) tSNE visualization of all cells from *LeprB-Cre;mTmG* control (purple) and *LeprB-Cre;mTmG;SmoM2*$^{+/-}$ mutant (green) samples.

(C) Unsupervised hierarchical clustering of all cells from control and mutant samples reveals 17 main cell types. Cycling EPI, cycling interfollicular keratinocytes; *Krt14*$^{+}$ EPI, *Krt14*$^{+}$ interfollicular keratinocytes; *Krt10*$^{+}$ EPI, *Krt10*$^{+}$ interfollicular keratinocytes; *Ivl*$^{+}$ EPI, *Ivl*$^{+}$ interfollicular keratinocytes; Upper HF, upper hair follicle keratinocytes; Lower HF, lower hair follicle keratinocytes; SG, sebaceous gland cells/sebocytes; FIB, dermal fibroblasts; DP/DP-like, dermal papilla/dermal papilla-like fibroblasts; FA-FIB, fibro-adipogenic fibroblasts; MUSC, muscle cells; ENDO, endothelial cells; LYM, lymphatic endothelial cells; NAEC, neuron-associated endothelial cells; IMM, immune cells; SCH, Schwann cells; and MEL, melanocytes.

(legend continued on next page)

ligand *Scube3* (Wu et al., 2011) (Figures 5C, 5D, 6A, 6B, 6H, S6C, S6D, and S8F). A change in non-canonical WNT pathway was dominantly dependent on activated *Wnt5a* expression in DPL II cells (Figures 4H, 5H, S4C, S6C, and S6D). Furthermore, a number of pathways that were inactive among control HF cells became activated in mutant (Figures S6B–S6D). These include IGF and VEGF pathways, driven by DPL II cells overexpressing *Igf1* and *Vegfa*, respectively (Figures 5E, 5F, 6A, 6B, and 6G). Other key hair-growth-modulating pathways, FGF and canonical WNT, underwent more subtle changes. FGF pathway remained functionally similar in mutant and control HFs (Figure 5G) but increased in strength, due to mutant DP fibroblasts overexpressing *Fgf7* and *Fgf10* ligands (Table S1). Canonical WNT pathway underwent several gene expression changes; however, their nature was such that they collectively preserved the pathway's functional similarity and somewhat reduced its strength in mutant samples (Figures S6B–S6E). On one hand, DPL fibroblasts expressed higher levels of WNT antagonists *Frzb, Ndk2*, and *Wif1* (Figures 6B and 6K; Table S1). On the other hand, mutant DP fibroblasts increased expression of WNT activators *Rspo1* and *Rspo3* and decreased inhibitory WNT ligand deacylase *Notum* (Figures 6B, 6I, and 6J; Table S1). Taken together, CellChat analysis suggests that mutant DPL II fibroblasts activate a distinct secretome, enriched for several hair growth-modulating ligands and antagonists that collectively and strongly promote hair-growth.

GRN features of Hedgehog-active fibroblasts

Next, we performed gene regulatory network (GRN) analysis on DP/DPL cells with pySCENIC (Van de Sande et al., 2020). DPL II cells clustered distinctly from the rest of DP fibroblasts (Figure 6C), suggesting a distinct regulon activity profile (Figure 6D; Table S2). Confirming transgenic stimulation of Hedgehog signaling, mutant DPL II cells strongly activated Gli1^{Reg}(+) regulon. Other top activated regulons included Hoxc8^{Reg}(+), Zfp239^{Reg}(+), Sox18^{Reg}(+), Alx3^{Reg}(+), and Ebf1^{Reg}(+) (Figures 6D and 6E). Among these, *Sox18* is a putative downstream target of Gli1^{Reg}(+), and *Hoxc8* is predicted to be downstream of Ebf1^{Reg}(+), Sox18^{Reg}(+), and Zfp239^{Reg}(+). Furthermore, several signaling genes upregulated in DPL II fibroblasts, including *Bmp4*, *Hhip*, *Igf1*, *Vegfa*, and *Scube3*, were predicted to be downstream of Gli1^{Reg}(+) regulon (Figure 6F). Thus, mutant DPL II fibroblasts activate redundant GRNs downstream of transgenically stimulated Gli1^{Reg}(+).

We also examined mutant-specific FA-FIB cells by comparing them with DS cells, with which they cluster closely (Figure 4D). Similar to DPL II fibroblasts, FA-FIBs upregulated core Hedgehog pathway genes (Figures S7A and S7B; Table S3) but expressed far fewer hair-growth-related signaling genes. These included *Ccl2*, *Igfbp4*, *Ngf*, *Wif1*, and *Wnt5b*. Among regulons, FA-FIBs strongly activated Gli1^{Reg}(+), pro-adipogenic Pparg^{Reg}(+), and Creb3l1^{Reg}(+) as well as Egr1^{Reg}(+) and Nelfe^{Reg}(+) regulons (Figures S7C and S7D). Several upregulated signaling genes listed above were predicted to be downstream of these core FA-FIB regulons (Figure S7E).

Next, we examined epithelial hair progenitors, which subcluster into two bulge SC and two HG populations (Figure S4D). In contrast to DP fibroblasts, epithelial hair progenitors in P46 *LeprB-Cre;SmoM2*$^{+/-}$ mice did not significantly alter their composition, and only a handful of genes were differentially expressed. The most notable changes were observed in mutant HG I cells, which downregulated several components of STAT3 pathway, including *Cish*, *Osmr*, *Pim1*, *Socs3*, and *Stat3* (Figures S7F and S7G; Table S4). Another notable change was upregulation in mutant HG I and Bulge II clusters of *Htra1* (Figures S7F and S7G; Table S4), a serine protease that can modulate FGF (Hou et al., 2007), BMP, and TGF-β signaling (Oka et al., 2004). Among regulons, mutant HG I cells decreased regulon activity of Bhlhe40^{Reg}(+), Egr2^{Reg}(+), Hoxa5^{Reg}(+), Klf9^{Reg}(+), and Klf13^{Reg}(+) (Figures S7H and S7I), which are the upstream regulators of the above listed STAT3 pathway genes and *Htra1* (Figure S7J). Considering that phosphorylated STAT3 marks epithelial hair progenitors during normal early telogen (Harel et al., 2015), we speculate that downregulation of STAT3 pathway components represents an early epithelial response event downstream of mutant DPL secretome.

SCUBE3 induces hair growth

Our analyses identified *Scube3* as the top upregulated signaling factor downstream of Gli1^{Reg}(+) regulon in DPL II fibroblasts. SCUBE3 is a multifunctional protein that can augment BMP (Lin et al., 2021) and FGF8 signaling (Tu et al., 2014) on source cells in its membrane-tethered form or TGF-β signaling in its proteolytically cleaved secreted form (Wu et al., 2011; Yang et al., 2007, 2020). In embryonic mouse skin, *Scube3* is preferentially expressed in DP and DS compartments of developing HFs (Haworth et al., 2007). Our re-analysis of published transcriptomic datasets from postnatal mouse skin showed that *Scube3* is highly and specifically expressed in DP fibroblasts from anagen but not telogen HFs (Figures S8A and S8B) and that it is also expressed by a subset of DS fibroblasts (Figure S8B). We then profiled *Scube3* expression pattern using RNAscope (Figure 7A). *Scube3* was highly expressed in DPs of P0 and P5 early anagen HFs, but then prominently decreased by P17, ahead of anagen termination. It was absent in first telogen HFs at P22, reappeared in second anagen HFs at P32 and then turned off again during

(D) Sub-clustering of all fibroblasts split by genotype (control on the left, mutant in the center) reveals 22 subclusters. Subcluster relatedness is shown on the bottom right.

(E) Feature plots of DP (left) and FA-FIB aggregate scores (right).

(F) Relative proportions of all fibroblast subclusters annotated in (D). Error bars represent standard deviation of the mean. **** $p < 0.00005$; *** $p < 0.0005$; * $p < 0.05$; n.s., no significance.

(G) Feature plots of *eGFP* expression (from *mTmG* transgene), *eYFP* expression (from *SmoM2-YFP* transgene) and Hedgehog (HH) signaling aggregate score (including ligands—blue and receptors—red) in all fibroblasts from control (top) and mutant (bottom) samples. HH signaling score was calculated based on normalized counts. Highly expressing subclusters are outlined.

(H) *In situ* expression of DPL marker *Wnt5a* (top two panels; red) and FA-FIB marker *Pcsk5* (bottom two panels; red) in both control and mutant skin at P46. Tissue sections were counterstained with DAPI.

Abbreviations: Norm. Cts., normalized counts. Scale bars, 100 μm in (H).

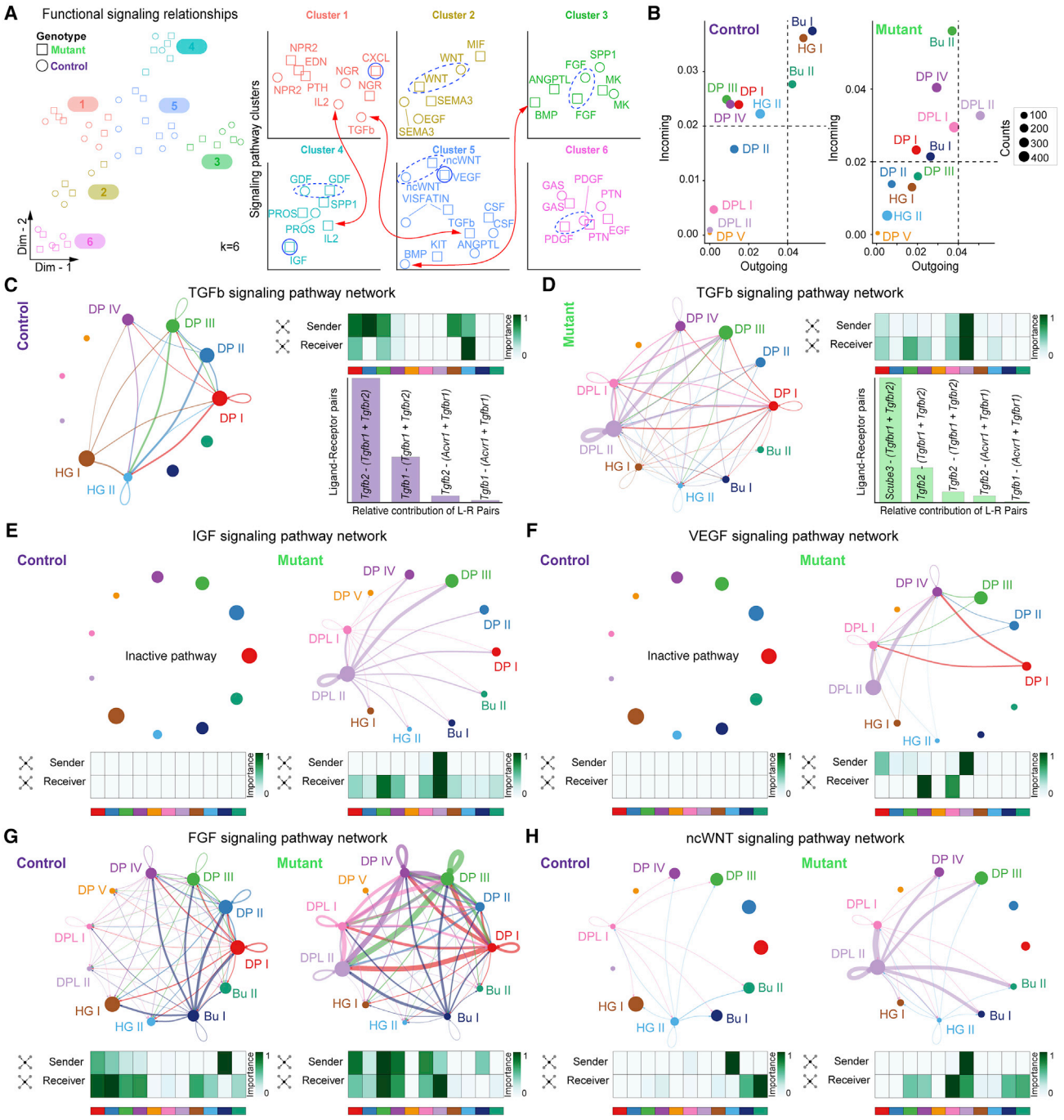

Figure 5. Dermal Hedgehog activation alters hair follicle signaling networks

(A) Functional relationship between significantly active signaling pathways among epithelial hair progenitors (bulge and HG cells) and DP/DPL fibroblasts for control (circles) and mutant samples (squares). Significantly active pathways organize into six clusters. Magnified view of clusters (right) demonstrates prominent changes in TGF-β and BMP pathways (red arrows). Pathways with preserved functional relationship include WNT, PDGF, GDF, and FGF (dotted outlines). Pathways that are significantly active only in the mutant sample include CXCL, VEGF, and IGF (solid outlines).

(B) Visualization of overall incoming and outgoing communication strength based on receptor and ligand expression in control (left) and mutant samples (right). Dot size is proportional to cells in each cluster.

(C and D) Inferred signaling networks for TGF-β pathway in control (C) and mutant HFs (D). Circle plots are shown on the left. Cell clusters that participate in signaling are annotated. Heatmaps showing relative importance of each HF cell cluster as signal sender or receiver are shown on the left/top right. Relative contribution of different ligand-receptor pairs to TGF-β signaling is shown on the left/bottom right.

(E–H) Circle plots and heatmaps of inferred signaling networks for IGF (E), VEGF (F), FGF (G), and ncWNT pathways (H) are shown. IGF and VEGF signaling pathways are scored as inactive in control HFs.

Abbreviations: DP, dermal papilla; DPL, dermal papilla-like; Bu, bulge; and HG, hair germ.

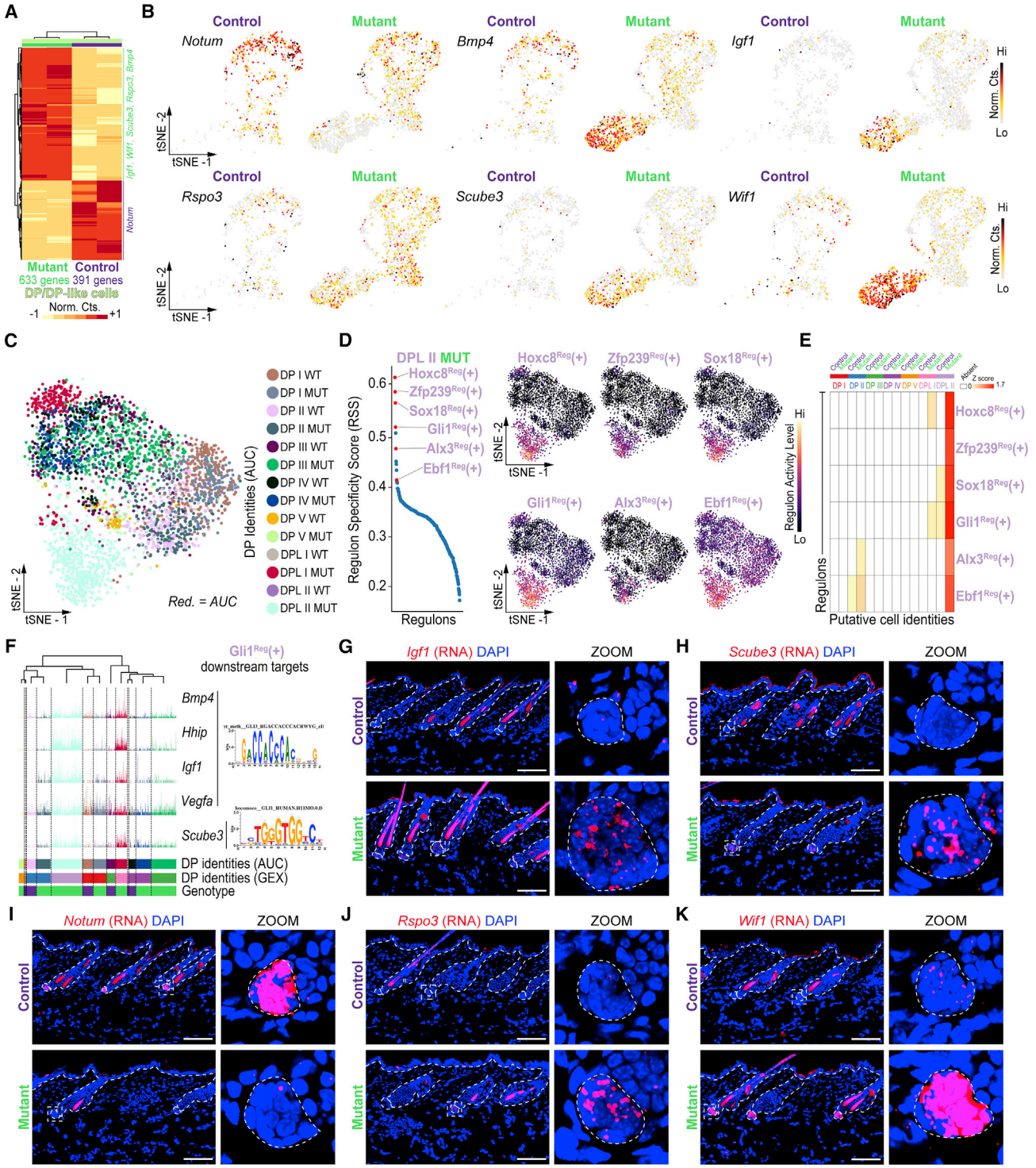

Figure 6. Hedgehog-regulated GRNs in dermal papilla fibroblasts

(A) Heatmap of differentially expressed genes (DEGs) between control and mutant DP/DPL fibroblasts. Number of DEGs are indicated, and selected genes are annotated on the right.

(B) Feature plots of selected DEGs in control versus mutant DP/DPL fibroblasts.

(C) AUC/regulon activity-based clustering of control and mutant DP/DPL fibroblasts overlaid on two-dimensional tSNE embedding.

(D) Rank of significantly active regulons in mutant fibroblasts from subcluster DPL II (left) based on regulon specificity score (RSS). Regulons of interest are annotated. Activity heatmaps (*Z* score >0) for selected mutant DPL II regulons are on the right.

(E) Activity heatmap of selected regulons from (C) and (D) across all DP subclusters, with control and mutant cells identified separately.

(legend continued on next page)

second telogen at P50. Scattered expression was also seen in hair matrix but only during first anagen phase. Thus, *Scube3* is an anagen phase-associated DP marker gene.

Next, we asked if SCUBE3 might exert anagen-promoting effect. When microinjected for 4 days starting at P48, recombinant human SCUBE3 (rhSCUBE3) induced significant hair growth in mouse back skin when compared on day 14 with bovine serum albumin (BSA) (Figures 7B and 7C). Aging in mice is associated with HF miniaturization (Matsumura et al., 2016) and increase in extrafollicular hair-growth inhibitors (Chen et al., 2014). To test if rhSCUBE3 can induce hair growth in aged skin, we repeated protein microinjections in 20-month-old mice. Unlike BSA, rhSCUBE3 potently stimulated hair growth (Figures 7D, 7E, and S8C). We also examined timing of second anagen initiation in dorsal skin of germline *Scube3*$^{-/-}$ mice, which are viable and develop grossly normal fur, despite having craniofacial defects (Lin et al., 2021). Compared with littermate controls, *Scube3*$^{-/-}$ mice show distinct, albeit mild anagen initiation delay (Figures S8D and S8E).

Next, we considered that hair-growth-promoting effect of SCUBE3 might be mediated via its target TGF-β pathway (Oshimori and Fuchs, 2012). We examined phosho-SMAD2 expression as an indicator of TGF-β activation. At P50, control telogen HFs showed virtually no phospho-SMAD2, in line with absent *Scube3* expression (Figure 7F, left). In contrast, P50 *LeprB-Cre;SmoM2*$^{+/-}$ HFs, whose morphology ranged from telogen-like to early anagen-like, showed prominent nuclear phospho-SMAD2 in HG cells and their derivatives as well as in the portion of bulge SCs (Figure 7F, right). Phospho-SMAD2^{+} HG cells were evident in mutant HFs already at P46 (Figure S8F). We then topically treated skin of *LeprB-Cre;SmoM2*$^{+/-}$ mice with SB525334, a potent TGF-β type I receptor inhibitor (Grygielko et al., 2005). Treatment of dorsal skin between P70 and P90 performed every other day resulted in near complete suppression of ectopic anagen HFs compared with vehicle-treated control mutant mice (Figures 7G, 7H, and S8G).

To start evaluating the translational potential of SCUBE3, we examined its expression pattern in human anagen HFs from occipital scalp. On RNAscope, *SCUBE3* is expressed in DP cells and strongly in the DS cup, a lowermost portion of DS (Figure 7K). We then xenografted human occipital scalp HFs to pigmented *SCID* mice and treated them with three daily doses of rhSCUBE3 or BSA on post-grafting day 30, when grafted human HFs enter telogen (Oh et al., 2016). Anagen phase human and adjacent mouse host HFs were then counted at each injection site on post-grafting day 50. Compared with BSA (n = 5), rhSCUBE3 (n = 6) accelerated anagen entry of grafted human HFs and stimulated new anagen by mouse host HFs (Figures 7I and 7J). We conclude that SCUBE3 is a mesenchymal niche-derived hair-growth activator in mice, whose expression pattern and function are at least partially conserved in human scalp.

DISCUSSION

Our findings lend several insights. First, we show that signaling regulation of fibroblast states is lineage specific. In skin, *LeprB-Cre* targets two distinct fibroblast populations, one in the DP and another in the dermal adipose layer. When Hedgehog signaling is upregulated in *LeprB-Cre;SmoM2*$^{+/-}$ mice, both fibroblast populations respond by expanding and forming new cell states. However, the molecular aspects of their responses are distinct and largely non-overlapping. Top regulons in DPL fibroblasts include known DP transcription factors Alx3^{Reg}(+), Ebf1^{Reg}(+), and Sox18^{Reg}(+) (Rezza et al., 2016; Villani et al., 2017), whereas top FA-FIB regulons include *bona fide* adipogenic Pparg^{Reg}(+) (Tontonoz et al., 1994) and smooth muscle contractile Egr1^{Reg}(+) (Santiago et al., 1999). Importantly and expectedly, both mutant DPL and FA-FIB fibroblasts turn on Hedgehog-dependent Gli1^{Reg}(+) regulon; however, its top Gli1^{Reg}(+) regulated overexpressed secretome genes are different. Thus, pre-existing lineage identity strongly affects the context of cellular response to the same signaling pathway. Maintaining contextual differences in signaling responses is important, since many distinct cell populations often coexist within small spatial scales and often within equal proximity from signaling sources. It enables signaling pathways to have multiple non-overlapping functions even in the same tissue.

Specific to HF biology, we show that *LeprB-Cre* and *Lepr-CreER* are reliable genetic tools for targeting DP fibroblasts. The latter constitute the key signaling niche for HF epithelial cells, and both *Cre* lines will enable future mechanistic studies into its biology. *LeprB*-based tools complement other existing *Cre* lines for targeting DPs; however, they offer critical advantages. Their *Cre* expression is driven by the *Lepr* isoform that has low abundance, enabling late onset, past the phase of HF morphogenesis. This allows to largely avoid developmental hair phenotypes even with a constitutive *Cre* version. Timing hair-growth phenotype onset to second telogen, which is normally long lasting (Greco et al., 2009; Plikus et al., 2008), simplifies interpretation, since a premature anagen around this time would be highly indicative of DP-induced HF SC activation. On the other hand, a delay in third anagen onset past P90 would be indicative of the loss of activating function by the HF niche.

Our results also lend new insight into the signaling hierarchy of hair-growth regulation. Normally, the decision by quiescent HFs to start new growth is tightly regulated at several levels, including intrinsically within epithelial hair SCs (Ezhkova et al., 2011; Flores et al., 2017; Horsley et al., 2008; Janich et al., 2011; Lee et al., 2021) and extrinsically by the immediate signaling niche, whose major component are DP fibroblasts (Avigad Laron et al., 2018; Enshell-Seijffers et al., 2010a; Hagner et al., 2020; Harshuk-Shabso et al., 2020; Rezza et al., 2016; Shin et al., 2020), as well as by skin macroenvironment, which includes long-range

(F) Trackplot showing expression patterns of selected target genes of Gli1^{Reg}(+) regulon across all DP subclusters. Genes are annotated on the right. Gene expression levels are represented on a per-cell basis by track height and are accompanied by their specific motifs on the right.
(G and H) Expression of selected Gli1^{Reg}(+) target genes—*Igf1* (G) and *Scube3* (H) in control (top) and mutant skin (bottom) at P46. DPs are magnified on the right.
(I–K) Expression of WNT pathway genes *Notum* (I), *Rspo3* (J), and *Wif1* (K) in control (top) and mutant skin (bottom) at P46. DPs are magnified on the right. Tissue sections were counterstained with DAPI.
Abbreviations: DP, dermal papilla; DPL, dermal papilla-like; Norm. Cts., normalized counts; AUC, area under the curve; and GEX, gene expression. Scale bars, 100 μm in (G–K).

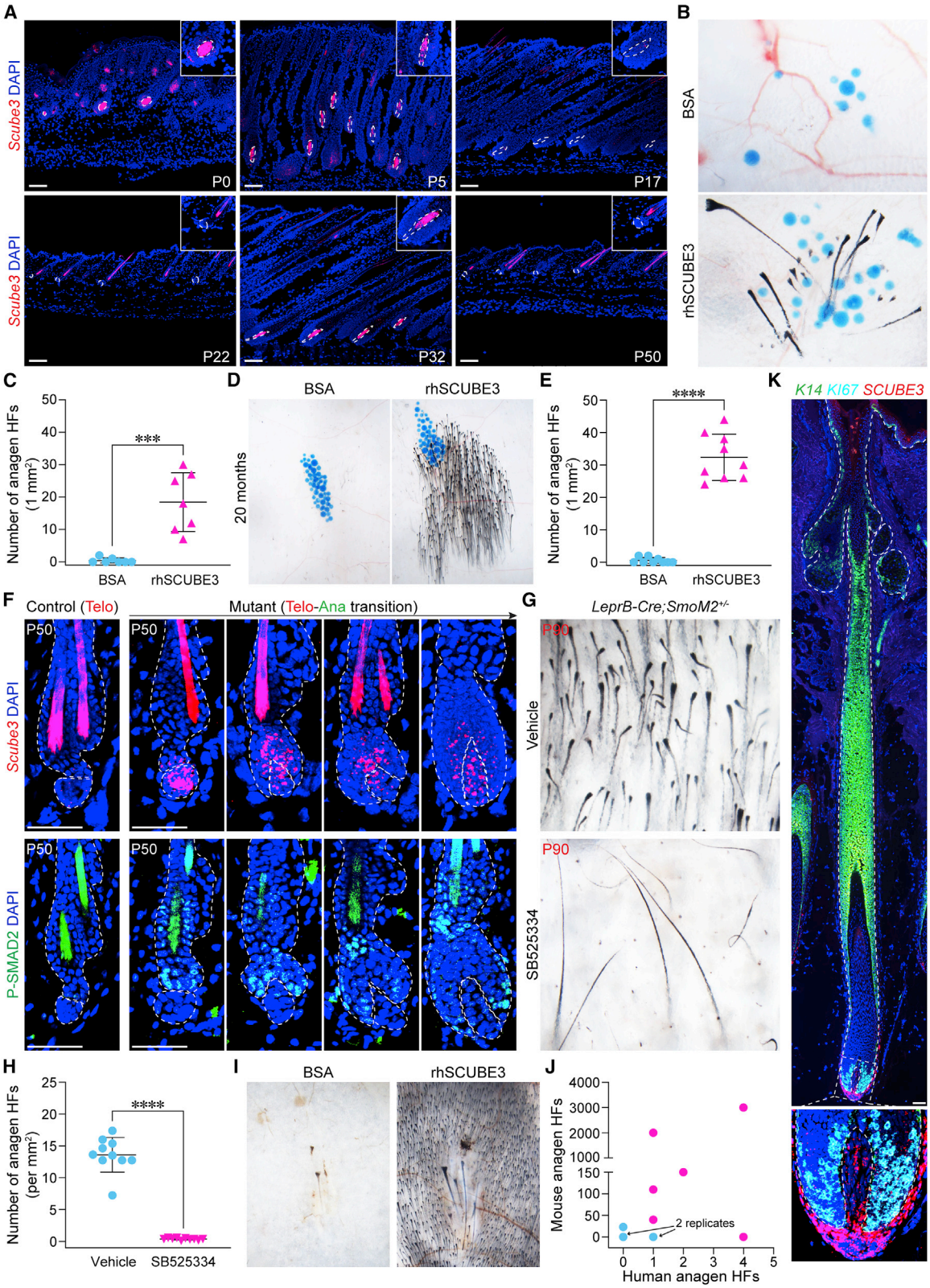

(legend on next page)

signals by dermal adipose cells (Chen et al., 2014; Festa et al., 2011; Plikus et al., 2008), immune cells (Ali et al., 2017; Chen et al., 2015; Wang et al., 2019), vascular cells (Gur-Cohen et al., 2019; Peña-Jimenez et al., 2019), and nerve endings (Brownell et al., 2011; Fujiwara et al., 2011; Shwartz et al., 2020). Our results show that over-activating the DP niche is sufficient to overcome normal mechanisms of HF quiescence, albeit only partially. One of the most distinctive features of *LeprB-Cre;SmoM2*$^{+/-}$ phenotype is that ectopic anagen HFs are interspersed with telogen HFs (Figure 3). This is distinct from normal hair growth in adult mice, which occurs in coordinated waves (Plikus et al., 2011; Plikus and Chuong, 2014). Normally, coordinated hair growth in mouse skin is prevented by the so-called refractory macroenvironment, which includes dermal adipose-derived BMP (Greco et al., 2009; Plikus et al., 2008; Zhang et al., 2019) and macrophage-derived Oncostatin-M (Wang et al., 2019), among other signals. When profiled in scRNA-seq data, refractory gene expression signature of skin microenvironment cells in mutant mice at P46 was not significantly lower than that in control mice (Figure S5A). This suggests that hair-growth regulation by signals originating outside of the HF is actually very important and that niche microenvironment "struggles" to override it even when niche is transgenically hyper-activated.

Our results identify SCUBE3 as a hair-growth activator. We show that physiological *Scube3* is expressed by DP fibroblasts only during anagen and that in mutant DPL fibroblasts, it becomes prominently upregulated. This overexpression is accompanied by precocious activation of TGF-β-specific phosho-SMAD2 in epithelial hair progenitors. We also show that SCUBE3 microinjection is sufficient to induce hair growth, whereas pharmacological TGF-β inhibition is sufficient to reverse ectopic hair growth in *LeprB-Cre;SmoM2*$^{+/-}$ mice. Intriguingly, SCUBE3 has a dual signaling function—in its native membrane-tethered form, it augments BMP signaling (Lin et al., 2021), whereas its secreted form drives TGF-β signaling (Wu et al., 2011; Yang et al., 2007, 2020). Our data suggest that the anagen-promoting effect of SCUBE3 is dependent upon its secreted form and upon downstream activation of TGF-β signaling. SCUBE3 can likely exert additional cell-autonomous and BMP-dependent effects on DP fibroblasts, and this will require further investigation. Indeed, BMP signaling in DP fibroblasts is normally required for their HF-inductive properties in cell grafting studies (Rendl et al., 2008).

Intriguing in this respect is the additional HF neogenesis phenotype observed in the skin of *LeprB-Cre;SmoM2*$^{+/-}$ mice (Figures 3E and 3F). Future mechanistic studies will be required to examine the role of SCUBE3 and/or other Hedgehog-dependent genes in HF neogenesis. Further studies will also be necessary to fully delineate minimal cellular targets for Hedgehog-induced HF neogenesis. As in skin wounds (Lim et al., 2018), fibroblast-specific Hedgehog stimulation appears to be sufficient for HF neogenesis in unwounded skin in our experiments. However, concomitant epidermal and dermal Hedgehog activation was shown to be required for HF neogenesis in another recent study (Sun et al., 2020). It is likely that the specific molecular approach to Hedgehog activation—*SmoM2* overexpression versus *Ptch1* deletion, as well as the choice of *Cre* driver—largely DP-specific *LeprB-Cre* versus pan-fibroblast *Col1a2-CreER*, may affect experimental outcomes. At the same time, our results suggest an exciting possibility that clinically desirable HF neogenesis in unwounded skin can be, in principle, achieved with only dermal Hedgehog activation, which would bypass tumorigenic potential associated with epithelial Hedgehog activation (Atwood et al., 2013; Fan et al., 1997).

Limitations of the study

Newly generated inducible *LeprB-CreER* mouse line enables specific reporter gene targeting in both telogen and anagen DP cells. However, future studies will be required to confirm its high efficiency for inducible gene deletion or overexpression. Our results suggest that anagen-promoting effect of SCUBE3 is TGF-β pathway dependent. However, considering multifunctional properties of SCUBE3 and related SCUBE1 and SCUBE2, their direct activating effects on other signaling pathways in the context of hair-growth regulation need to be further explored.

STAR★METHODS

Detailed methods are provided in the online version of this paper and include the following:

- KEY RESOURCES TABLE
- RESOURCE AVAILABILITY
  - Lead contact

Figure 7. SCUBE3 induces hair growth

(A) Expression of pan-isoform *Scube3* mRNA (red) in normal mouse skin.

(B) Representative images of microinjection sites for BSA (top) and rhSCUBE3 (bottom). Affi-gel agarose beads (blue) are visible. Newly growing anagen HFs are pigmented.

(C) Quantification of induced anagen HFs in response to rhSCUBE3 on day 14 post-injection. Mean difference is 18 ± 3.44; n = 7; *** $p < 0.001$.

(D) Representative images of microinjection sites for BSA (left) and rhSCUBE3 (right) on 20-month-old mice.

(E) Quantification of induced anagen HFs in aged mice on day 14 after protein injection. Mean difference is 31.78 ± 2.40; n = 9; **** $p < 0.0001$.

(F) *Scube3* mRNA (red, top) and phospho-SMAD2 expression (green, bottom) in control (left) and mutant HFs (right) at P50.

(G) Whole-mount images of P90 mutant skin topically treated with vehicle (left) and SB525334 (right) for 20 days.

(H) Quantification of anagen HF density per mm^2 in mutant skin topically treated with vehicle or SB525334. Each dot represents one randomly selected skin area. Mean difference is 13.22 ± 0.86; n = 10; **** $p < 0.0001$.

(I) Representative images of microinjection sites for BSA and rhSCUBE3 in human occipital scalp HF-on-SCID mouse xenograft model.

(J) Scattered plot of human and mouse anagen HF quantification. Red dots represent rhSCUBE3-injected samples and blue dots represent BSA-injected samples.

(K) Expression of *K14*, *KI67*, and *SCUBE3* mRNAs in human anagen occipital scalp HF. *SCUBE3* mRNA is specifically and highly expressed in DP and adjacent dermal sheath cup. Tissue sections were counterstained with DAPI in (A), (F), and (K).

Abbreviations: rhSCUBE3, recombinant human SCUBE3 and BSA, bovine serum albumin. Scale bars, 50 μm in (A, F, and K).

SUPPLEMENTAL INFORMATION

Supplemental information can be found online at https://doi.org/10.1016/j.devcel.2022.06.005.

ACKNOWLEDGMENTS

M.V.P. is supported by LEO Foundation grants LF-AW-RAM-19-400008 and LF-OC-20-000611, Chan Zuckerberg Initiative grant AN-0000000062, W.M. Keck Foundation grant WMKF-5634988, NSF grant DMS1951144, and NIH grants U01-AR073159, R01-AR079470, R01-AR079150, R21-AR078939, and P30-AR075047. Additional support comes from the NSF grant DMS1763272 and Simons Foundation grant (594598, Q.N.). J.L. is supported by the Training Program of the Major Research Plan of the National Natural Science Foundation of China (91749114) and National Natural Science Foundation of China (81773351); Y.L. by the National Natural Science Foundation of China (82073467); R.-B.Y. by Ministry of Science and Technology of Taiwan (MOST 109-2320-B-001-012-MY3); Y.-C.L. by MOST 110-2326-B-001-004-MY3; C.F.G.-J. by UC Irvine Chancellor's ADVANCE Postdoctoral Fellowship Program, NSF-Simons Postdoctoral Fellowship (DMS1763272, to Q.N.), Simons Foundation grant (594598, to Q.N.), and by a generous gift from the HHMI Hanna H. Gray Postdoctoral Fellowship Program; L.J.M.L. by UC-MEXUS CONACYT and Fullbright-Garcia Robles doctoral fellowships. The authors would like to thank Shenghan Chen and Junyu Nan for their help with mouse husbandry and genotyping.

AUTHOR CONTRIBUTIONS

Y.L., C.F.G.-J., and M.V.P. conceptualized research; M.V.P. and J.L. supervised research; Y.L., C.F.G.-J., F.X., N.U.S., R.R., C.-H.K., and R.L. performed research; L.J.M.L. performed statistical analysis; Y.L. and C.F.G.-J. implemented computational and bioinformatic tools and algorithms for 3′ single-cell RNA-seq analyses; Y.L. and C.F.G.-J. performed 3′ single-cell RNA sequencing and bioinformatic analyses and curated data; Y.L. and C.F.G.-J. designed and generated figures; Y.-C.L., S.-J.L., M.T., R.-B.Y., Z.Y., Q.N., and M.V.P. contributed reagents and analytic tools; Q.N. supervised 3′ single-cell RNA sequencing and bioinformatic analyses and data curation; J.M.P. and J.W.O performed whole-mount imaging and analysis; Y.L., C.F.G.-J., and M.V.P. wrote the manuscript; J.L. and Q.N. edited the manuscript.

DECLARATION OF INTERESTS

Y.L., C.F.G.-J., and M.V.P. have filed a provisional patent describing hair-growth promoting properties of SCUBE3 and its related proteins.

Received: May 4, 2021
Revised: March 10, 2022
Accepted: June 8, 2022
Published: June 30, 2022

REFERENCES

Abbasi, S., Sinha, S., Labit, E., Rosin, N.L., Yoon, G., Rahmani, W., Jaffer, A., Sharma, N., Hagner, A., Shah, P., et al. (2020). Distinct regulatory programs control the latent regenerative potential of dermal fibroblasts during wound healing. Cell Stem Cell *27*, 396–412.e6.

Ali, N., Zirak, B., Rodriguez, R.S., Pauli, M.L., Truong, H.A., Lai, K., Ahn, R., Corbin, K., Lowe, M.M., Scharschmidt, T.C., et al. (2017). Regulatory T cells in skin facilitate epithelial stem cell differentiation. Cell *169*, 1119–1129.e11.

Atwood, S.X., Li, M., Lee, A., Tang, J.Y., and Oro, A.E. (2013). GLI activation by atypical protein kinase C ι/λ regulates the growth of basal cell carcinomas. Nature *494*, 484–488.

Avigad Laron, E., Aamar, E., and Enshell-Seijffers, D. (2018). The mesenchymal niche of the hair follicle induces regeneration by releasing primed progenitors from inhibitory effects of quiescent stem cells. Cell Rep. *24*, 909–921.e3.

Bergen, V., Lange, M., Peidli, S., Wolf, F.A., and Theis, F.J. (2020). Generalizing RNA velocity to transient cell states through dynamical modeling. Nat. Biotechnol. *38*, 1408–1414.

Biggs, L.C., Mäkelä, O.J., Myllymäki, S.M., Das Roy, R., Närhi, K., Pispa, J., Mustonen, T., and Mikkola, M.L. (2018). Hair follicle dermal condensation forms via FGF20 primed cell cycle exit, cell motility, and aggregation. eLife *7*, e36468.

Botchkarev, V.A., Botchkareva, N.V., Nakamura, M., Huber, O., Funa, K., Lauster, R., Paus, R., and Gilchrest, B.A. (2001). Noggin is required for induction of the hair follicle growth phase in postnatal skin. FASEB J. *15*, 2205–2214.

Brownell, I., Guevara, E., Bai, C.B., Loomis, C.A., and Joyner, A.L. (2011). Nerve-derived sonic hedgehog defines a niche for hair follicle stem cells capable of becoming epidermal stem cells. Cell Stem Cell *8*, 552–565.

Chen, C.C., Murray, P.J., Jiang, T.X., Plikus, M.V., Chang, Y.T., Lee, O.K., Widelitz, R.B., and Chuong, C.M. (2014). Regenerative hair waves in aging mice and extra-follicular modulators follistatin, dkk1, and sfrp4. J. Invest. Dermatol. *134*, 2086–2096.

Chen, C.C., Wang, L., Plikus, M.V., Jiang, T.X., Murray, P.J., Ramos, R., Guerrero-Juarez, C.F., Hughes, M.W., Lee, O.K., Shi, S., et al. (2015). Organ-level quorum sensing directs regeneration in hair stem cell populations. Cell *161*, 277–290.

Chi, W., Wu, E., and Morgan, B.A. (2013). Dermal papilla cell number specifies hair size, shape and cycling and its reduction causes follicular decline. Development *140*, 1676–1683.

Chiang, C., Swan, R.Z., Grachtchouk, M., Bolinger, M., Litingtung, Y., Robertson, E.K., Cooper, M.K., Gaffield, W., Westphal, H., Beachy, P.A., and Dlugosz, A.A. (1999). Essential role for Sonic hedgehog during hair follicle morphogenesis. Dev. Biol. *205*, 1–9.

Clavel, C., Grisanti, L., Zemla, R., Rezza, A., Barros, R., Sennett, R., Mazloom, A.R., Chung, C.Y., Cai, X., Cai, C.L., et al. (2012). Sox2 in the dermal papilla

niche controls hair growth by fine-tuning BMP signaling in differentiating hair shaft progenitors. Dev. Cell *23*, 981–994.

Correa-Gallegos, D., Jiang, D., Christ, S., Ramesh, P., Ye, H., Wannemacher, J., Kalgudde Gopal, S., Yu, Q., Aichler, M., Walch, A., et al. (2019). Patch repair of deep wounds by mobilized fascia. Nature *576*, 287–292.

DeFalco, J., Tomishima, M., Liu, H., Zhao, C., Cai, X., Marth, J.D., Enquist, L., and Friedman, J.M. (2001). Virus-assisted mapping of neural inputs to a feeding center in the hypothalamus. Science *291*, 2608–2613.

Driskell, R.R., Clavel, C., Rendl, M., and Watt, F.M. (2011). Hair follicle dermal papilla cells at a glance. J. Cell Sci. *124*, 1179–1182.

Driskell, R.R., Lichtenberger, B.M., Hoste, E., Kretzschmar, K., Simons, B.D., Charalambous, M., Ferron, S.R., Herault, Y., Pavlovic, G., Ferguson-Smith, A.C., and Watt, F.M. (2013). Distinct fibroblast lineages determine dermal architecture in skin development and repair. Nature *504*, 277–281.

Enshell-Seijffers, D., Lindon, C., Kashiwagi, M., and Morgan, B.A. (2010a). Beta-catenin activity in the dermal papilla regulates morphogenesis and regeneration of hair. Dev. Cell *18*, 633–642.

Enshell-Seijffers, D., Lindon, C., Wu, E., Taketo, M.M., and Morgan, B.A. (2010b). Beta-catenin activity in the dermal papilla of the hair follicle regulates pigment-type switching. Proc. Natl. Acad. Sci. USA *107*, 21564–21569.

Ezhkova, E., Lien, W.H., Stokes, N., Pasolli, H.A., Silva, J.M., and Fuchs, E. (2011). EZH1 and EZH2 cogovern histone H3K27 trimethylation and are essential for hair follicle homeostasis and wound repair. Genes Dev. *25*, 485–498.

Fan, H., Oro, A.E., Scott, M.P., and Khavari, P.A. (1997). Induction of basal cell carcinoma features in transgenic human skin expressing Sonic Hedgehog. Nat. Med. *3*, 788–792.

Fan, J., Salathia, N., Liu, R., Kaeser, G.E., Yung, Y.C., Herman, J.L., Kaper, F., Fan, J.B., Zhang, K., Chun, J., and Kharchenko, P.V. (2016). Characterizing transcriptional heterogeneity through pathway and gene set overdispersion analysis. Nat. Methods *13*, 241–244.

Festa, E., Fretz, J., Berry, R., Schmidt, B., Rodeheffer, M., Horowitz, M., and Horsley, V. (2011). Adipocyte lineage cells contribute to the skin stem cell niche to drive hair cycling. Cell *146*, 761–771.

Flores, A., Schell, J., Krall, A.S., Jelinek, D., Miranda, M., Grigorian, M., Braas, D., White, A.C., Zhou, J.L., Graham, N.A., et al. (2017). Lactate dehydrogenase activity drives hair follicle stem cell activation. Nat. Cell Biol. *19*, 1017–1026.

Fujiwara, H., Ferreira, M., Donati, G., Marciano, D.K., Linton, J.M., Sato, Y., Hartner, A., Sekiguchi, K., Reichardt, L.F., and Watt, F.M. (2011). The basement membrane of hair follicle stem cells is a muscle cell niche. Cell *144*, 577–589.

Gat, U., DasGupta, R., Degenstein, L., and Fuchs, E. (1998). De novo hair follicle morphogenesis and hair tumors in mice expressing a truncated beta-catenin in skin. Cell *95*, 605–614.

Gay, D., Ghinatti, G., Guerrero-Juarez, C.F., Ferrer, R.A., Ferri, F., Lim, C.H., Murakami, S., Gault, N., Barroca, V., Rombeau, I., et al. (2020). Phagocytosis of Wnt inhibitor SFRP4 by late wound macrophages drives chronic Wnt activity for fibrotic skin healing. Sci. Adv. *6*, eaay3704.

Ge, W., Tan, S.J., Wang, S.H., Li, L., Sun, X.F., Shen, W., and Wang, X. (2020). Single-cell transcriptome profiling reveals dermal and epithelial cell fate decisions during embryonic hair follicle development. Theranostics *10*, 7581–7598.

González, R., Moffatt, G., Hagner, A., Sinha, S., Shin, W., Rahmani, W., Chojnacki, A., and Biernaskie, J. (2017). Platelet-derived growth factor signaling modulates adult hair follicle dermal stem cell maintenance and self-renewal. NPJ Regen. Med. *2*, 11.

Gorska, E., Popko, K., Stelmaszczyk-Emmel, A., Ciepiela, O., Kucharska, A., and Wasik, M. (2010). Leptin receptors. Eur. J. Med. Res. *15* (*Suppl 2*), 50–54.

Greco, V., Chen, T., Rendl, M., Schober, M., Pasolli, H.A., Stokes, N., Dela Cruz-Racelis, J., and Fuchs, E. (2009). A two-step mechanism for stem cell activation during hair regeneration. Cell Stem Cell *4*, 155–169.

Grygielko, E.T., Martin, W.M., Tweed, C., Thornton, P., Harling, J., Brooks, D.P., and Laping, N.J. (2005). Inhibition of gene markers of fibrosis with a novel inhibitor of transforming growth factor-beta type I receptor kinase in puromycin-induced nephritis. J. Pharmacol. Exp. Ther. *313*, 943–951.

Guerrero-Juarez, C.F., Dedhia, P.H., Jin, S., Ruiz-Vega, R., Ma, D., Liu, Y., Yamaga, K., Shestova, O., Gay, D.L., Yang, Z., et al. (2019). Single-cell analysis reveals fibroblast heterogeneity and myeloid-derived adipocyte progenitors in murine skin wounds. Nat. Commun. *10*, 650.

Gupta, K., Levinsohn, J., Linderman, G., Chen, D., Sun, T.Y., Dong, D., Taketo, M.M., Bosenberg, M., Kluger, Y., Choate, K., and Myung, P. (2019). Single-cell analysis reveals a hair follicle dermal niche molecular differentiation trajectory that begins prior to morphogenesis. Dev. Cell *48*, 17–31.e6.

Gur-Cohen, S., Yang, H., Baksh, S.C., Miao, Y., Levorse, J., Kataru, R.P., Liu, X., de la Cruz-Racelis, J., Mehrara, B.J., and Fuchs, E. (2019). Stem cell-driven lymphatic remodeling coordinates tissue regeneration. Science *366*, 1218–1225.

Hagner, A., Shin, W., Sinha, S., Alpaugh, W., Workentine, M., Abbasi, S., Rahmani, W., Agabalyan, N., Sharma, N., Sparks, H., et al. (2020). Transcriptional profiling of the adult hair follicle mesenchyme reveals R-spondin as a novel regulator of dermal progenitor function. iScience *23*, 101019.

Harel, S., Higgins, C.A., Cerise, J.E., Dai, Z., Chen, J.C., Clynes, R., and Christiano, A.M. (2015). Pharmacologic inhibition of JAK-STAT signaling promotes hair growth. Sci. Adv. *1*, e1500973.

Harshuk-Shabso, S., Dressler, H., Niehrs, C., Aamar, E., and Enshell-Seijffers, D. (2020). Fgf and Wnt signaling interaction in the mesenchymal niche regulates the murine hair cycle clock. Nat. Commun. *11*, 5114.

Hawkshaw, N.J., Hardman, J.A., Alam, M., Jimenez, F., and Paus, R. (2020). Deciphering the molecular morphology of the human hair cycle: Wnt signalling during the telogen-anagen transformation. Br. J. Dermatol. *182*, 1184–1193.

Haworth, K., Smith, F., Zoupa, M., Seppala, M., Sharpe, P.T., and Cobourne, M.T. (2007). Expression of the Scube3 epidermal growth factor-related gene during early embryonic development in the mouse. Gene Expr. Patterns *7*, 630–634.

Heitman, N., Sennett, R., Mok, K.W., Saxena, N., Srivastava, D., Martino, P., Grisanti, L., Wang, Z., Ma'ayan, A., Rompolas, P., and Rendl, M. (2020). Dermal sheath contraction powers stem cell niche relocation during hair cycle regression. Science *367*, 161–166.

Horsley, V., Aliprantis, A.O., Polak, L., Glimcher, L.H., and Fuchs, E. (2008). NFATc1 balances quiescence and proliferation of skin stem cells. Cell *132*, 299–310.

Hou, S., Maccarana, M., Min, T.H., Strate, I., and Pera, E.M. (2007). The secreted serine protease xHtrA1 stimulates long-range FGF signaling in the early *Xenopus* embryo. Dev. Cell *13*, 226–241.

Hsu, Y.C., Pasolli, H.A., and Fuchs, E. (2011). Dynamics between stem cells, niche, and progeny in the hair follicle. Cell *144*, 92–105.

Ito, M., Yang, Z., Andl, T., Cui, C., Kim, N., Millar, S.E., and Cotsarelis, G. (2007). Wnt-dependent de novo hair follicle regeneration in adult mouse skin after wounding. Nature *447*, 316–320.

Janich, P., Pascual, G., Merlos-Suárez, A., Batlle, E., Ripperger, J., Albrecht, U., Cheng, H.Y., Obrietan, K., Di Croce, L., and Benitah, S.A. (2011). The circadian molecular clock creates epidermal stem cell heterogeneity. Nature *480*, 209–214.

Jin, S., Guerrero-Juarez, C.F., Zhang, L., Chang, I., Ramos, R., Kuan, C.H., Myung, P., Plikus, M.V., and Nie, Q. (2021). Inference and analysis of cell-cell communication using CellChat. Nat. Commun. *12*, 1088.

Joost, S., Annusver, K., Jacob, T., Sun, X., Dalessandri, T., Sivan, U., Sequeira, I., Sandberg, R., and Kasper, M. (2020). The molecular anatomy of mouse skin during hair growth and rest. Cell Stem Cell *26*, 441–457.e7.

Kim, D., Chen, R., Sheu, M., Kim, N., Kim, S., Islam, N., Wier, E.M., Wang, G., Li, A., Park, A., et al. (2019). Noncoding dsRNA induces retinoic acid synthesis to stimulate hair follicle regeneration via TLR3. Nat. Commun. *10*, 2811.

LeBleu, V.S., and Neilson, E.G. (2020). Origin and functional heterogeneity of fibroblasts. FASEB J. *34*, 3519–3536.

Lee, S.A., Li, K.N., and Tumbar, T. (2021). Stem cell-intrinsic mechanisms regulating adult hair follicle homeostasis. Exp. Dermatol. *30*, 430–447.

Legrand, J.M.D., Roy, E., Ellis, J.J., Francois, M., Brooks, A.J., and Khosrotehrani, K. (2016). STAT5 activation in the dermal papilla is important for hair follicle growth phase induction. J. Invest. Dermatol. *136*, 1781–1791.

Lim, C.H., Sun, Q., Ratti, K., Lee, S.H., Zheng, Y., Takeo, M., Lee, W., Rabbani, P., Plikus, M.V., Cain, J.E., et al. (2018). Hedgehog stimulates hair follicle neogenesis by creating inductive dermis during murine skin wound healing. Nat. Commun. *9*, 4903.

Lin, Y.C., Niceta, M., Muto, V., Vona, B., Pagnamenta, A.T., Maroofian, R., Beetz, C., van Duyvenvoorde, H., Dentici, M.L., Lauffer, P., et al. (2021). SCUBE3 loss-of-function causes a recognizable recessive developmental disorder due to defective bone morphogenetic protein signaling. Am. J. Hum. Genet. *108*, 115–133.

Lo Celso, C., Prowse, D.M., and Watt, F.M. (2004). Transient activation of beta-catenin signalling in adult mouse epidermis is sufficient to induce new hair follicles but continuous activation is required to maintain hair follicle tumours. Development *131*, 1787–1799.

Love, M.I., Huber, W., and Anders, S. (2014). Moderated estimation of fold change and dispersion for RNA-seq data with DESeq2. Genome Biol. *15*, 550.

Lynch, M.D., and Watt, F.M. (2018). Fibroblast heterogeneity: implications for human disease. J. Clin. Invest. *128*, 26–35.

Matsumura, H., Mohri, Y., Binh, N.T., Morinaga, H., Fukuda, M., Ito, M., Kurata, S., Hoeijmakers, J., and Nishimura, E.K. (2016). Hair follicle aging is driven by transepidermal elimination of stem cells via COL17A1 proteolysis. Science *351*, aad4395.

Mok, K.W., Saxena, N., Heitman, N., Grisanti, L., Srivastava, D., Muraro, M.J., Jacob, T., Sennett, R., Wang, Z., Su, Y., et al. (2019). Dermal condensate niche fate specification occurs prior to formation and is placode progenitor dependent. Dev. Cell *48*, 32–48.e5.

Morgan, B.A. (2014). The dermal papilla: an instructive niche for epithelial stem and progenitor cells in development and regeneration of the hair follicle. Cold Spring Harb. Perspect. Med. *4*, a015180.

Oh, J.W., Kloepper, J., Langan, E.A., Kim, Y., Yeo, J., Kim, M.J., Hsi, T.C., Rose, C., Yoon, G.S., Lee, S.J., et al. (2016). A guide to studying human hair follicle cycling in vivo. J. Invest. Dermatol. *136*, 34–44.

Oka, C., Tsujimoto, R., Kajikawa, M., Koshiba-Takeuchi, K., Ina, J., Yano, M., Tsuchiya, A., Ueta, Y., Soma, A., Kanda, H., et al. (2004). HtrA1 serine protease inhibits signaling mediated by Tgfbeta family proteins. Development *131*, 1041–1053.

Oshimori, N., and Fuchs, E. (2012). Paracrine TGF-beta signaling counterbalances BMP-mediated repression in hair follicle stem cell activation. Cell Stem Cell *10*, 63–75.

Paladini, R.D., Saleh, J., Qian, C., Xu, G.X., and Rubin, L.L. (2005). Modulation of hair growth with small molecule agonists of the hedgehog signaling pathway. J. Invest. Dermatol. *125*, 638–646.

Peña-Jimenez, D., Fontenete, S., Megias, D., Fustero-Torre, C., Graña-Castro, O., Castellana, D., Loewe, R., and Perez-Moreno, M. (2019). Lymphatic vessels interact dynamically with the hair follicle stem cell niche during skin regeneration in vivo. EMBO J. *38*, e101688.

Phan, Q.M., Fine, G.M., Salz, L., Herrera, G.G., Wildman, B., Driskell, I.M., and Driskell, R.R. (2020). Lef1 expression in fibroblasts maintains developmental potential in adult skin to regenerate wounds. eLife *9*, e60066.

Philippeos, C., Telerman, S.B., Oulès, B., Pisco, A.O., Shaw, T.J., Elgueta, R., Lombardi, G., Driskell, R.R., Soldin, M., Lynch, M.D., and Watt, F.M. (2018). Spatial and single-cell transcriptional profiling identifies functionally distinct human dermal fibroblast subpopulations. J. Invest. Dermatol. *138*, 811–825.

Plikus, M.V., Baker, R.E., Chen, C.C., Fare, C., de la Cruz, D., Andl, T., Maini, P.K., Millar, S.E., Widelitz, R., and Chuong, C.M. (2011). Self-organizing and stochastic behaviors during the regeneration of hair stem cells. Science *332*, 586–589.

Plikus, M.V., and Chuong, C.M. (2014). Macroenvironmental regulation of hair cycling and collective regenerative behavior. Cold Spring Harb. Perspect. Med. *4*, a015198.

Plikus, M.V., Guerrero-Juarez, C.F., Ito, M., Li, Y.R., Dedhia, P.H., Zheng, Y., Shao, M., Gay, D.L., Ramos, R., Hsi, T.C., et al. (2017). Regeneration of fat cells from myofibroblasts during wound healing. Science *355*, 748–752.

Plikus, M.V., Mayer, J.A., de la Cruz, D., Baker, R.E., Maini, P.K., Maxson, R., and Chuong, C.M. (2008). Cyclic dermal BMP signalling regulates stem cell activation during hair regeneration. Nature *451*, 340–344.

Plikus, M.V., Wang, X., Sinha, S., Forte, E., Thompson, S.M., Herzog, E.L., Driskell, R.R., Rosenthal, N., Biernaskie, J., and Horsley, V. (2021). Fibroblasts: origins, definitions, and functions in health and disease. Cell *184*, 3852–3872.

Rahmani, W., Abbasi, S., Hagner, A., Raharjo, E., Kumar, R., Hotta, A., Magness, S., Metzger, D., and Biernaskie, J. (2014). Hair follicle dermal stem cells regenerate the dermal sheath, repopulate the dermal papilla, and modulate hair type. Dev. Cell *31*, 543–558.

Rendl, M., Polak, L., and Fuchs, E. (2008). BMP signaling in dermal papilla cells is required for their hair follicle-inductive properties. Genes Dev. *22*, 543–557.

Rezza, A., Wang, Z., Sennett, R., Qiao, W., Wang, D., Heitman, N., Mok, K.W., Clavel, C., Yi, R., Zandstra, P., et al. (2016). Signaling networks among stem cell precursors, transit-amplifying progenitors, and their niche in developing hair follicles. Cell Rep. *14*, 3001–3018.

Rinkevich, Y., Walmsley, G.G., Hu, M.S., Maan, Z.N., Newman, A.M., Drukker, M., Januszyk, M., Krampitz, G.W., Gurtner, G.C., Lorenz, H.P., et al. (2015). Skin fibrosis. Identification and isolation of a dermal lineage with intrinsic fibrogenic potential. Science *348*, aaa2151.

Rompolas, P., Deschene, E.R., Zito, G., Gonzalez, D.G., Saotome, I., Haberman, A.M., and Greco, V. (2012). Live imaging of stem cell and progeny behaviour in physiological hair-follicle regeneration. Nature *487*, 496–499.

Santiago, F.S., Lowe, H.C., Kavurma, M.M., Chesterman, C.N., Baker, A., Atkins, D.G., and Khachigian, L.M. (1999). New DNA enzyme targeting Egr-1 mRNA inhibits vascular smooth muscle proliferation and regrowth after injury. Nat. Med. *5*, 1264–1269.

Sato, N., Leopold, P.L., and Crystal, R.G. (1999). Induction of the hair growth phase in postnatal mice by localized transient expression of Sonic hedgehog. J. Clin. Invest. *104*, 855–864.

Sennett, R., and Rendl, M. (2012). Mesenchymal-epithelial interactions during hair follicle morphogenesis and cycling. Semin. Cell Dev. Biol. *23*, 917–927.

Sennett, R., Wang, Z., Rezza, A., Grisanti, L., Roitershtein, N., Sicchio, C., Mok, K.W., Heitman, N.J., Clavel, C., Ma'ayan, A., and Rendl, M. (2015). An integrated transcriptome atlas of embryonic hair follicle progenitors, their niche, and the developing skin. Dev. Cell *34*, 577–591.

Shin, W., Rosin, N.L., Sparks, H., Sinha, S., Rahmani, W., Sharma, N., Workentine, M., Abbasi, S., Labit, E., Stratton, J.A., and Biernaskie, J. (2020). Dysfunction of hair follicle mesenchymal progenitors contributes to age-associated hair loss. Dev. Cell *53*, 185–198.e7.

Shook, B.A., Wasko, R.R., Mano, O., Rutenberg-Schoenberg, M., Rudolph, M.C., Zirak, B., Rivera-Gonzalez, G.C., López-Giráldez, F., Zarini, S., Rezza, A., et al. (2020). Dermal adipocyte lipolysis and myofibroblast conversion are required for efficient skin repair. Cell Stem Cell *26*, 880–895.e6.

Shook, B.A., Wasko, R.R., Rivera-Gonzalez, G.C., Salazar-Gatzimas, E., López-Giráldez, F., Dash, B.C., Muñoz-Rojas, A.R., Aultman, K.D., Zwick, R.K., Lei, V., et al. (2018). Myofibroblast proliferation and heterogeneity are supported by macrophages during skin repair. Science *362*, eaar2971.

Shwartz, Y., Gonzalez-Celeiro, M., Chen, C.L., Pasolli, H.A., Sheu, S.H., Fan, S.M., Shamsi, F., Assaad, S., Lin, E.T., Zhang, B., et al. (2020). Cell types promoting goosebumps form a niche to regulate hair follicle stem cells. Cell *182*, 578–593.e19.

St-Jacques, B., Dassule, H.R., Karavanova, I., Botchkarev, V.A., Li, J., Danielian, P.S., McMahon, J.A., Lewis, P.M., Paus, R., and McMahon, A.P. (1998). Sonic hedgehog signaling is essential for hair development. Curr. Biol. *8*, 1058–1068.

Stuart, T., Butler, A., Hoffman, P., Hafemeister, C., Papalexi, E., Mauck, W.M., 3rd, Hao, Y., Stoeckius, M., Smibert, P., and Satija, R. (2019). Comprehensive integration of single-cell data. Cell *177*, 1888–1902.e21.

Subramanian, A., Tamayo, P., Mootha, V.K., Mukherjee, S., Ebert, B.L., Gillette, M.A., Paulovich, A., Pomeroy, S.L., Golub, T.R., Lander, E.S., and Mesirov, J.P. (2005). Gene set enrichment analysis: a knowledge-based approach for interpreting genome-wide expression profiles. Proc. Natl. Acad. Sci. USA *102*, 15545–15550.

Sun, X., Are, A., Annusver, K., Sivan, U., Jacob, T., Dalessandri, T., Joost, S., Füllgrabe, A., Gerling, M., and Kasper, M. (2020). Coordinated hedgehog signaling induces new hair follicles in adult skin. eLife *9*, e46756.

Tabib, T., Morse, C., Wang, T., Chen, W., and Lafyatis, R. (2018). SFRP2/DPP4 and FMO1/LSP1 define major fibroblast populations in human skin. J. Invest. Dermatol. *138*, 802–810.

Telerman, S.B., Rognoni, E., Sequeira, I., Pisco, A.O., Lichtenberger, B.M., Culley, O.J., Viswanathan, P., Driskell, R.R., and Watt, F.M. (2017). Dermal Blimp1 acts downstream of epidermal TGFbeta and Wnt/beta-catenin to regulate hair follicle formation and growth. J. Invest. Dermatol. *137*, 2270–2281.

Tontonoz, P., Hu, E., and Spiegelman, B.M. (1994). Stimulation of adipogenesis in fibroblasts by PPAR gamma 2, a lipid-activated transcription factor. Cell *79*, 1147–1156.

Tu, C.F., Tsao, K.C., Lee, S.J., and Yang, R.B. (2014). SCUBE3 (signal peptide-CUB-EGF domain-containing protein 3) modulates fibroblast growth factor signaling during fast muscle development. J. Biol. Chem. *289*, 18928–18942.

Van de Sande, B., Flerin, C., Davie, K., De Waegeneer, M., Hulselmans, G., Aibar, S., Seurinck, R., Saelens, W., Cannoodt, R., Rouchon, Q., et al. (2020). A scalable SCENIC workflow for single-cell gene regulatory network analysis. Nat. Protoc. *15*, 2247–2276.

Villani, R., Hodgson, S., Legrand, J., Greaney, J., Wong, H.Y., Pichol-Thievend, C., Adolphe, C., Wainwight, B., Francois, M., and Khosrotehrani, K. (2017). Dominant-negative Sox18 function inhibits dermal papilla maturation and differentiation in all murine hair types. Development *144*, 1887–1895.

Wang, E.C.E., Dai, Z., Ferrante, A.W., Drake, C.G., and Christiano, A.M. (2019). A subset of TREM2^{+} dermal macrophages secretes oncostatin M to maintain hair follicle stem cell quiescence and inhibit hair growth. Cell Stem Cell *24*, 654–669.e6.

Wang, Q., Oh, J.W., Lee, H.L., Dhar, A., Peng, T., Ramos, R., Guerrero-Juarez, C.F., Wang, X., Zhao, R., Cao, X., et al. (2017). A multi-scale model for hair follicles reveals heterogeneous domains driving rapid spatiotemporal hair growth patterning. eLife *6*, e22772.

Wolbert, J., Li, X., Heming, M., Mausberg, A.K., Akkermann, D., Frydrychowicz, C., Fledrich, R., Groeneweg, L., Schulz, C., Stettner, M., et al. (2020). Redefining the heterogeneity of peripheral nerve cells in health and autoimmunity. Proc. Natl. Acad. Sci. USA *117*, 9466–9476.

Wolock, S.L., Lopez, R., and Klein, A.M. (2019). Scrublet: computational identification of cell doublets in single-cell transcriptomic data. Cell Syst. *8*, 281–291.e9.

Woo, W.M., Zhen, H.H., and Oro, A.E. (2012). Shh maintains dermal papilla identity and hair morphogenesis via a Noggin-Shh regulatory loop. Genes Dev. *26*, 1235–1246.

Wu, Y.Y., Peck, K., Chang, Y.L., Pan, S.H., Cheng, Y.F., Lin, J.C., Yang, R.B., Hong, T.M., and Yang, P.C. (2011). SCUBE3 is an endogenous TGF-beta receptor ligand and regulates the epithelial-mesenchymal transition in lung cancer. Oncogene *30*, 3682–3693.

Yang, H.Y., Cheng, C.F., Djoko, B., Lian, W.S., Tu, C.F., Tsai, M.T., Chen, Y.H., Chen, C.C., Cheng, C.J., and Yang, R.B. (2007). Transgenic overexpression of the secreted, extracellular EGF-CUB domain-containing protein SCUBE3 induces cardiac hypertrophy in mice. Cardiovasc. Res. *75*, 139–147.

Yang, X., Hu, J., Shi, C., and Dai, J. (2020). Activation of TGF-beta1 pathway by SCUBE3 regulates TWIST1 expression and promotes breast cancer progression. Cancer Biother. Radiopharm. *35*, 120–128.

Zhang, Z., Shao, M., Hepler, C., Zi, Z., Zhao, S., An, Y.A., Zhu, Y., Ghaben, A.L., Wang, M.Y., Li, N., et al. (2019). Dermal adipose tissue has high plasticity and undergoes reversible dedifferentiation in mice. J. Clin. Invest. *129*, 5327–5342.

Zhou, L., Xu, M., Yang, Y., Yang, K., Wickett, R.R., Andl, T., Millar, S.E., and Zhang, Y. (2016). Activation of beta-catenin signaling in CD133-positive dermal papilla cells drives postnatal hair growth. PLoS One *11*, e0160425.

STAR★METHODS

KEY RESOURCES TABLE

REAGENT or RESOURCE	SOURCE	IDENTIFIER
Antibodies		
Chicken anti-KRT14	Xing Dai Laboratory, University of California, Irvine	N/A
Rabbit anti-LEF1	Cell Signaling	C12A5
Goat anti-PDGFRa	R&D systems	AF1062
Rat anti-CD31	BD Bioscience	550274
Rat anti-CD45	BD Bioscience	553076
Rabbit anti-Ki67	Cell Signaling	9129
Rabbit anti-PLIN	Cell Signaling	9349S
Rabbit anti-pSMAD2	Cell Signaling	18338
Zombie NIR™ Fixable Viability Kit	Biolegend	423105
Chemicals, Peptides, and Recombinant Proteins		
Tamoxifen	Sigma-Aldrich	T5648
Recombinant human SCUBE3 Protein	R&D systems	7730-SC-050
TGFβ receptor I inhibitor (SB525334)	Selleckchem	S1476
Critical Commercial Assays		
RNAscope multiplex fluorescent detection kit v2	Advanced Cell Diagnostics	323100
Pan-isoform mouse *Lepr* probe	Advanced Cell Diagnostics	402731-C2
Customized mouse *LeprB*-specific probe	Advanced Cell Diagnostics	813871
Mouse *Wnt5a*-specific probe	Advanced Cell Diagnostics	316791-C2
Mouse *Pcsk5*-specific probe	Advanced Cell Diagnostics	901011-C3
Mouse *Wif1*-specific probe	Advanced Cell Diagnostics	412361-C3
Mouse *Igf1*-specific probe	Advanced Cell Diagnostics	443901-C3
Mouse *Scube3*-specific probe	Advanced Cell Diagnostics	488151
Mouse *Notum*-specific probe	Advanced Cell Diagnostics	428981
Mouse *Rspo3*-specific probe	Advanced Cell Diagnostics	402011-C2
Human *Hs-KRT14*-specific probe	Advanced Cell Diagnostics	310191-C3
Human *Hs-MKI67*-specific probe	Advanced Cell Diagnostics	591771
Human *Hs-SCUBE3*-specific probe	Advanced Cell Diagnostics	503841-C2
Tissue Clearing Starter's kit	Binaree, Korea	HRTC 101
Mounting and Storage solution	Binaree, Korea	HRTC 101-3
Dead cell removal kit	Myltenyi Biotec	130-090-101
Chromium Single Cell 3' GEM, Library and Gel Bead Kit v2	10X Genomics	PN-120237
Chromium Single Cell 3' GEM, Library and Gel Bead Kit v3	10X Genomics	PN-1000075
Deposited Data		
Mouse 3'-single-cell RNA-seq data (GFP^+ sorted and unsorted whole skin cells)	This manuscript	GSE160513
Experimental Models: Organisms/Strains		
C57BL/6J	The Jackson Laboratories	000664
C57BL/6J SCID	The Jackson Laboratories	001913
LeprB-Cre	The Jackson Laboratories	008320
Lepr-CreER	This manuscript	This manuscript

(*Continued on next page*)

Continued

REAGENT or RESOURCE	SOURCE	IDENTIFIER
Scube3$^{-/-}$	Ruey-Bing Yang Laboratory, Academia Sinica, Taiwan	https://pubmed.ncbi.nlm.nih.gov/23383134/
R26R	The Jackson Laboratories	003474
ROSA$^{mT/mG}$	The Jackson Laboratories	007676
ROSA^{tdTomato}	The Jackson Laboratories	007914
R26-SmoM2	Scott Atwood Laboratory, University of California, Irvine	https://pubmed.ncbi.nlm.nih.gov/15107405/
K14-H2BGFP	Elaine Fuchs Laboratory, Rockefeller University	Elaine Fuchs https://pubmed.ncbi.nlm.nih.gov/14671312/
Software and Algorithms		
R Studio	https://rstudio.com/products/rstudio/	Version 3.6.1
MATLAB	https://www.mathworks.com	Version R1028b
Python	https://www.python.org	Version 2.7.2; 3.7.0
Anaconda	https://anaconda.org	Version 3.6-5.0.1
Spyder (Python-IDE)	https://www.spyder-ide.org	Version 4.1.5
Samtools	https://github.com/samtools/	Version 1.9; 1.10
STAR	https://github.com/alexdobin/STAR	Version 2.5.1b
RSEM	https://github.com/deweylab/RSEM	Version 1.3.2
Cell Ranger	https://github.com/10XGenomics/cellranger	Version 2.1.1; 3.1.0
Scrublet	https://github.com/AllonKleinLab/scrublet	Version 0.2.1
Scanpy	https://github.com/theislab/scanpy	Version 1.4.4; 1.5.0
Seurat	https://github.com/satijalab/seurat	Version 3.2.2; 4.0.0
DESeq2	https://bioconductor.org/packages/release/bioc/html/DESeq2.html	Version 1.40.0
Velocyto	https://velocyto.org	Version 0.17.17
Loompy	http://loompy.org	Version 2.0.16
scVelo	https://github.com/theislab/scvelo	Version 0.2.2
CellChat	https://github.com/sqjin/CellChat	Version 0.5.0
pySCENIC	https://github.com/aertslab/pySCENIC	Version 0.10.2
Prism	https://www.graphpad.com/scientific-software/prism/	Version 9.2.0 (283)

RESOURCE AVAILABILITY

Lead contact

Further information and requests for resources and reagents should be directed to and will be fulfilled by the Lead Contact, Maksim Plikus (plikus@uci.edu).

Materials availability

Transgenic mouse strains generated in this study are available upon request.

Data and code availability

scRNA-seq datasets have been deposited in the Gene Expression Omnibus (GEO) database under the accession code: GSE160513 and are publicly available as of the date of publication. Any additional information required to reanalyze the data reported in this paper are available upon request.

EXPERIMENTAL MODEL AND SUBJECT DETAILS

Mice

The following mouse lines were used in this study: C57BL6/J (JAX stock 000664), *LeprB-Cre* (JAX stock 008320), *R26R* (JAX stock 003474), *ROSA*$^{mT/mG}$ *(mTmG)* (JAX stock 007676), *ROSA*^{tdTomato} *(tdTomato)* (JAX stock 007914), *R26-SmoM2 (SmoM2)* (donated by Dr. Scott Atwood, UC Irvine), and *Scube3*$^{-/-}$ (provided by Dr. Ruey-Bing Yang, Academia Sinica). *K14-H2BGFP* mice were obtained

from Elaine Fuchs laboratory at Rockefeller University under MTA. *LeprB-CreER* mice were generated by Shanghai Model Organisms Center (Shanghai, China). Briefly, *IRES-iCreERT2* construct was inserted after exon 19 stop codon of *Lepr* gene (Figure 2E). Only female mice were used in this study. All animal experiments were performed in compliance with the guidelines of the Institutional Animal Care and Use Committee (IACUC) of the University of California, Irvine. Animals were regularly monitored for any health concerns. All experimental animals were housed in a specific pathogen free facility in ventilated cages kept under 12-hour light and 12-hour dark cycle and food and water was provided *ad libitum*. The temperature in the facility was maintained between 70-74 °F.

Human tissue

Human occipital scalp tissues for histological analysis were collected from a 66-year-old Caucasian male. Human occipital hair follicles used in xenograft experiments were collected from a 33-year-old Caucasian male. Human tissues were obtained under IRB protocol approved by the University of California, Irvine and subjects gave informed consent for use of the tissue sample for research purposes.

METHOD DETAILS

Hair cycle tracing

LeprB-Cre;SmoM2$^{+/-}$, *Scube3*$^{-/-}$ and their control littermate mice were shaved during the first telogen and hair cycle status was monitored non-invasively on the basis of skin pigmentation changes as described previously (Plikus et al., 2008). Photographs were taken every 1-to-3 days and dorsal hair was shaved repeatedly.

Wholemount imaging

LeprB-Cre;SmoM2$^{+/-}$*;K14-H2BGFP* dorsal skin samples were fixed with 4% PFA overnight at 4°C and rinsed with 1x PBS. Tissues were then cleared with Tissue Clearing Starter's kit (HRTC 101, Binaree, Korea). Briefly, tissues were incubated in starting solution at 4°C for 24 hours and immersed with tissue clearing solution on a rotator at 37°C for 48 hours, and then washed four times with distilled water at 4°C for 1 hour. The clearing step was repeated. Tissues were then incubated in Mounting and Storage solution (HRTC 101-3) at 25°C for 24 hours and imaged using Zeiss confocal laser scanning microscope with a plan-apochromat 20x/0.8 M27 lens. Serial images were reconstructed using Imaris software (version 9.5.1).

LacZ staining

To detect β-Galactosidase activity on whole mount, freshly dissected skin samples were incubated with X-gal reagent in lacZ staining buffer, as previously reported (Plikus et al., 2017). Samples were post-fixed in 4% PFA and rinsed with 1x PBS. To detect β-Galactosidase activity on sections, skin samples were snap-frozen in OCT compound on dry ice. The frozen blocks were sectioned at 20 μm thickness. Tissue slides were post-fixed with 4% PFA for 10 mins, incubated with lacZ staining reagent for 18 hours and then rinsed with 1x PBS. Fast red solution was used for nuclei counterstaining. Whole mount samples were imaged with Nikon SMZ1500 dissecting microscope and tissue sections with Nikon Ti-E widefield microscope.

Histology and immunohistochemistry

Tissues were snap-frozen, embedded in OCT, and sectioned at 10 μm thickness. For histology, tissue sections were stained with hematoxylin and eosin. For immunostaining, tissue sections were post-fixed with 4% PFA for 10 mins and blocked with 2% BSA for 1 hour. The following primary antibodies were used: chicken anti-KRT14 (1:1000, gift from Dr. Xing Dai, UC Irvine), rabbit anti-LEF1(1:200, Cell Signaling), goat anti-PDGFRa (1:350, R&D), rat anti-CD31 (1:200, BD Bioscience), rat anti-CD45 (1:200, BD Bioscience), rabbit anti-Ki67 (1:1000, Cell Signaling), rabbit anti-PLIN (1:1000, Cell Signaling), rabbit anti-phospho-SMAD2 (1:250, Cell Signaling). DAPI was used for nuclei counterstaining. Tissue sections were visualized with an Olympus FV3000 confocal laser scanning microscope.

Tamoxifen induction

LeprB-CreER;tdTomato mice were injected with tamoxifen (Sigma-Aldrich, T5648) intra-peritoneally (0.1 mg/g diluted in corn oil, Sigma-Aldrich, C8267) for 5 consecutive days starting at postnatal days P21, P32 or P50. Skin was collected on day 6 after initial tamoxifen injection. Wholemount samples were fixed with 4% PFA overnight and then cleared with 50% glycerol. Tissue slides were fixed with 4% PFA for 10 mins and DAPI was used for nuclei counterstaining. Wholemount samples were imaged with Leica DM6 B microscope and tissue sections with a Nikon A1 confocal laser scanning microscope.

RNA *in situ* hybridization

Frozen tissue sections were processed for RNA *in situ* hybridization using the RNAscope multiplex fluorescent detection kit v2 (323100, Advanced Cell Diagnostics, ACD) according to manufacturer's protocol with minor modifications. The following ACD probes were used: *mouse probes* – pan-isoform *Lepr* (402731-C2), isoform-specific *LeprB* (813871), *Wnt5a* (316791-C2), *Pcsk5* (901011-C3), *Wif1* (412361-C3), *Igf1* (443901-C3), *Scube3* (488151), *Notum* (428981), and *Rspo3* (402011-C2); *human probes* – Hs-KRT14-C3 (310191-C3), Hs-MKI67 (591771), and Hs-SCUBE3-C2 (503841-C2). Chicken anti-KRT14 immunostaining (1:1000)

was performed together with *Lepr* probe detection according to manufacturer's instructions with minor modifications. DAPI was used for nuclei counterstaining. Images were acquired on an Olympus FV3000 confocal laser scanning microscope.

Topical inhibitor treatment

SB525334, a TGFβ type I receptor inhibitor (Selleck Chemicals) was diluted to a concentration of 20 mg/ml in ethanol. P70 *LeprB-Cre;SmoM2*$^{+/-}$ mice were treated with 50 μl of SB525334 solution topically on their dorsum every other day for twenty days. Skin was then collected and processed for whole mount imaging and histology.

Intradermal recombinant protein injections

Intradermal injections of recombinant human SCUBE3 (rhSCUBE3) protein were performed as previously described (Plikus et al., 2008). Briefly, rhSCUBE3 (R&D Systems) was reconstituted in 0.1% BSA to a final concentration of 250 μg/ml. Affi-gel blue agarose beads (Bio-Rad) were washed three times in sterile 1x PBS, air dried, and resuspended with rhSCUBE3 or BSA. Beads were micro-implanted into dorsal skin using a 26G needle at P48. Beads were resupplied with recombinant proteins at 24, 48, and 72 hours using a glass microneedle injector. Skin was analyzed on day 14 after initial bead micro-implantation.

Human HF xenograft model

Human occipital scalp HFs were xenografted as previously reported (Oh et al., 2016). Briefly, 4 to 6 anagen phase occipital scalp HFs were transplanted to the dorsal skin of 6-to-8-week-old female *SCID* mice. 30 days post-grafting, once human HFs enter transplantation-induced telogen, 10 μl of rhSCUBE3 or BSA control (250 μg/ml) were microinjected for 3 consecutive days. Host mice were sacrificed on post-grafting day 50. Wholemount skin samples were fixed with 4% PFA overnight and cleared with 50% glycerol. Images were taken with a Nikon SMZ1500 dissecting microscope.

Single cell isolation

Dorsal skin was harvested from female *LeprB-Cre;mTmG;SmoM2*$^{+/-}$ mutant and *LeprB-Cre;mTmG* littermate control mice at P46, when HFs are in telogen. Skin was micro-dissected, minced, and incubated in Dispase II/Collagenase IV/Liberase solution with constant rotation at 37°C for 1 hour. Cell aggregates were further dissociated using GentleMACS (MACS). Single cell suspensions were depleted of dead cells using Dead Cell Removal Kit (Myltenyi Biotec). Resulting live cells were quantified using a hemocytometer and further diluted to ~1,000 cells/μl.

In another experiment, GFP$^+$ cells were purified using fluorescence-activated cell sorting (FACS). Dorsal skin of *LeprB-Cre;mTmG* mice was collected at P50. Skin was micro-dissected, minced, and digested with 2 mg/ml Collagenase at 37°C with constant rotation for 1 hour and further disaggregated into single cells with 0.25% Trypsin at 37°C for 10 minutes. Single cell suspension was stained with Zombie NIR (1:1000, BioLegend) and FACS-sorted as Zombie$^-$/GFP$^+$ with a BD FACSAria II flow cytometer (BD Biosciences). Resulting live cells were quantified using a hemocytometer and further diluted to ~1,000 cells/μl.

Single-cell RNA-sequencing

Whole skin unsorted cells or sorted GFP$^+$ cells were captured using Chromium Platform and processed using Single Cell 3' v2 (for GFP$^+$ cells) and v3 (for whole skin unsorted cells) chemistries (10X Genomics). cDNA libraries were sequenced on Illumina HiSeq4000 (100 PE, GFP$^+$ cells) or NovaSeq (100 PE, whole skin unsorted cells). Cell capture, RT, cDNA library preparation and sequencing were performed at the Genomics High Throughput Facility at UC Irvine.

Processing of raw sequencing data

GFP$^+$ cells from LeprB-Cre;mTmG mice

Raw FASTQ reads were mapped to a modified version of the mouse mm10 reference genome (GRCm38.93.dna/GRCm38.93.gtf) using Cell Ranger Version 2.1.1. Briefly, the mm10 genome and GTF annotations were modified to include *GFP* nucleotide sequence as exon (1-5,556 nts) with the following common gene, transcript ID and name: *"eGFP".* The web summary alignment metrics were as follows: total number of reads: 119,459,349; reads mapped to genome: 89.4%; reads mapped confidently to the genome: 86.8%; reads confidently mapped to transcriptome: 66.7%; estimated number of cells: 455; fraction of reads in cells: 80.7%; mean reads per cells: 262,548; median genes per cell: 1,076; total genes detected: 14,853; median UMI counts per cell: 2,201.

Whole skin unsorted cells from LeprB-Cre;mTmG and LeprB-Cre;mTmG;SmoM2$^{+/-}$ mice

Raw FASTQ reads were mapped to a modified version of the mouse mm10 reference genome (GRCm38.94.dna/GRCm38.84.gtf) using Cell Ranger Version 3.1.0. Briefly, the mm10 genome and GTF annotations were modified to include the *GFP* (1-5,556 nts), *YFP* (1-720 nts), and *tdTomato* (1-719 nts) nucleotide sequences as exons with the following common gene, transcript IDs and names: *"eGFP", "YFP",* and *"tomato",* respectively. The web summary alignment metrics were as follows; *LeprB-Cre;mTmG* – replicate 1: total number of reads: 1,019,926,632; reads mapped to genome: 95.3%; reads mapped confidently to the genome: 91.7%; reads confidently mapped to transcriptome: 57.0%; estimated number of cells: 10,748; fraction of reads in cells: 93.5%; mean reads per cells: 94,895; median genes per cell: 2,160; total genes detected: 22,151; median UMI counts per cell: 6,832; *LeprB-Cre;mTmG* – replicate 2: total number of reads: 1,201,904,183; reads mapped to genome: 95.6%; reads mapped confidently to the genome: 92.0%; reads confidently mapped to transcriptome: 56.9%; estimated number of cells: 11,072; fraction of reads in cells: 93.5%; mean reads per cells: 108,553; median genes per cell: 2,143; total genes detected: 22,216; median UMI counts per cell: 6,750;

LeprB-Cre;mTmG;SmoM2$^{+/-}$ – replicate 1: total number of reads: 1,153,873,375; reads mapped to genome: 95.3%; reads mapped confidently to the genome: 91.6%; reads confidently mapped to transcriptome: 56.3%; estimated number of cells: 11,563; fraction of reads in cells: 91.3%; mean reads per cells: 99,790; median genes per cell: 2,128; total genes detected: 22,271; median UMI counts per cell: 6,335; *LeprB-Cre;mTmG;SmoM2*$^{+/-}$ – replicate 2: total number of reads: 1,160,592,293; reads mapped to genome: 95.5%; reads mapped confidently to the genome: 91.9%; reads confidently mapped to transcriptome: 56.1%; estimated number of cells: 11,816; fraction of reads in cells: 91.9%; mean reads per cells: 98,222; median genes per cell: 2,105; total genes detected: 22,275; median UMI counts per cell: 6,198.

Doublet/multiplet simulation and low-quality cell pruning

Raw, digitized count matrices were pre-processed and doublet/multiplets of type A and B were simulated using Single-Cell Remover of Doublets (Scrublet) (Wolock et al., 2019) (version 0.2.1) with the following parameters enabled: *scrub.scrub_doublets* (min_counts=2, min_cells=3, min_gene_variability_pctl=85, n_prin_comps=30). The doublet/multiplet score threshold was adjusted manually to be consistent with the intersection of the bimodal distribution of the observed transcriptomes on the probability density histogram as suggested by developer. The resultant AnnData object was exported as compressed AnnData H5AD file (Scanpy version 1.4.4). AnnData H5AD files were read in Seurat for downstream low-quality cell pruning. Only whole skin unsorted cells were subjected to doublet/multiplet removal. Singlet GFP-positive and whole skin unsorted cells were kept and used for downstream query analyses iff they met the following collective quality control metrics: a) 350 < genes/cell < 5,000; b) cells contained no more than 10% (GFP$^+$ sorted cells) or 20% (whole skin unsorted cells) of mitochondrial gene expression; c) cells were not identified as outliers falling outside a prediction confidence interval as defined in Pagoda (p-value 1e^{-3}) (Fan et al., 2016).

Bioinformatic analysis of GFP$^+$ cells

A Seurat object was created using a raw, digitized counts matrix (Version 3.2.2, R Studio version 3.6.1) (Stuart et al., 2019). The raw, digitized counts matrix was Log-normalized and variable genes/features were identified using the *FindVariableFeatures* function with the following parameters enabled: *selection.method* = "*mean.var.plot*", mean.cutoff = c(0.0125, 3) and *dispersion.cutoff* = *c(0.5, Inf)*. The object was then scaled using the *ScaleData* function. Significant PCs used for clustering and neighbor finding were identified using a combination of statistical (PC heatmaps and Jackstraw method – 100 permutations) and heuristic methods (elbow plot). Neighbors and clusters were identified using the *FindNeighbors* and *FindClusters* functions, respectively, with dimensions specified by the user and visualized using t-distributed Stochastic Neighbor Embedding (tSNE). Gene biomarkers (cluster markers) were identified by establishing a minimum average Log Fold Change requirement (min.pct) of 25% and a minimum of 25% (tresh.use) cells that must express such gene biomarker in either one cluster. Gene biomarkers were identified using the *FindAllMarkers* function using the Wilcoxon Rank Sum Test (Wilcoxon). Gene biomarkers were Log-normalized and visualized in two-dimensional feature plots. Cell identities were assigned based on *bona fide* biomarker gene expression.

Anchoring, integration, and downstream analysis

We performed anchoring and integration of control and mutant whole skin unsorted single-cell data sets using the Seurat package (Version 3.2.2, R Studio version 3.6.1) (Stuart et al., 2019). Briefly, Seurat objects were created using individual, raw digitized count matrices. Objects were then merged with the *merge* function. Individual gene expression digital matrices were normalized and variable genes/features were identified using the *FindVariableFeatures* function with the *selection.method* = *"vst"* and *nfeatures* = *2000* parameters enabled. Integration anchors were identified using the *FindIntegrationAnchors* function with dimensions set to 30. Data sets were subsequently integrated using the *IntegrateData* function with dimensions set to 30. The integrated object was scaled using the *ScaleData* function. Significant PCs used for clustering and finding neighbors were identified using a combination of statistical and heuristic methods as before. Neighbors and clusters were identified using the *FindNeighbors* and *FindClusters* functions with dimensions specified by user and visualized using t-distributed Stochastic Neighbor Embedding (tSNE) with Barnes-Hut approximation. Putative cell types were identified based on biomarker gene expression (cluster markers) by establishing a minimum average Log Fold Change requirement (min.pct) of 25% and a minimum of 25% (tresh.use) cells that must express such gene biomarker in either one cluster. Gene biomarkers were identified using the *FindAllMarkers* function with the Wilcoxon Rank Sum Test (Wilcoxon). Gene biomarkers were Log-normalized and visualized as feature plots. Cell type identities were assigned based on *bona fide* biomarker gene expression. To determine whether there are statistically significant changes in cell type cluster composition across genotypes, we averaged the cells per cluster of interest by technical replicate and performed a two-sample proportion test (alpha = 0.05). We implemented a Bonferroni correction to account for multiple hypothesis testing.

Agglomerative hierarchical clustering

Agglomerative hierarchical clustering based on Euclidian distance with Ward's linkage was performed on selected cell types using the MATLAB function *plot_Cladogram* with gene-cell normalized raw counts and cluster specific identities as input.

Differential Gene Expression analysis

Differentially expressed genes between cell types or cell clusters across genotypes were calculated using a DESeq2 pipeline tailored for scRNA-seq data sets (Love et al., 2014). Briefly, raw counts were modeled for each gene using size factors to account for differences in library sequencing depth. Gene-wise dispersions were then estimated and shrunk to generate accurate dispersion

estimates. We then fitted a negative binomial model to the data and performed hypothesis testing with the Wald Test. Differentially expressed genes for a particular comparison were filtered using a P-adjusted threshold of 0.05 and a Log_2 fold-change of 0.58 or greater in either direction.

LeprB isoform analysis

Bulk RNA-seq datasets from Rezza et al. (2016) were downloaded from Gene Expression Omnibus (accession number GSE77197). Single-end (SE) reads were aligned to a reference mouse genome (mm10/genocode.vM8) using STAR version 2.5.1b with the following parameters: *'–outFilterMismatchNmax 10 –outFilterMismatchNoverReadLmax 0.07 –outFilterMultimapNmax 10'.* Gene and isoform expression levels were quantified using RSEM v.1.3.2 with expression values normalized into Fragments Per Kilobase of transcript per Million mapped reads (FPKM).

Reference mapping

We performed asymmetric dataset integration using ingest (Scanpy version 1.5.0) from an annotated reference (*LeprB-Cre;mTmG;SmoM2*$^{+/-}$ (SMO mutant) DP/DP-like fibroblasts) into distinct query datasets, including embryonic day 14.5 dermal condensate fibroblasts (Gupta et al., 2019), P2 DP fibroblasts (Phan et al., 2020), anagen/telogen DP/DS fibroblasts (Joost et al., 2020), Hedgehog-activated small wound dermal fibroblasts (Lim et al., 2018), and post-wounding day 14 wound center *Rspo3*$^{+}$ fibroblasts (Abbasi et al., 2020). We used *LeprB-Cre;mTmG* DP fibroblasts as ''internal query control''. Briefly, datasets were defined on the same variables and the model and graphs were trained on the reference dataset independently. Query datasets were mapped onto the reference data with a pre-existing two-dimensional Uniform Manifold Approximation and Projection (UMAP) embedding.

Marker gene module scoring

Aggregate marker gene module scores were assigned to DP/DP-like, DS, FA-FIB, bulge SCs, NAECs, and refractory and competent telogen using the *AddModuleScore* function in Seurat with the following conditions enabled: ctrl = 2.5 or 5. DP/DP-like cells were identified by implementation of a *"DP aggregate score"* defined by a core set of known DP-associated marker genes, including *Agouti* (*a*), *Rspo3, Prlr*, and *Bmp4*; DS cells – by known DS-associated markers, including *Acta2*, *Tagln*, *Mylk*, and *Ramp1*; FA-FIB – by known fibro-adipogenic markers, including *Acta2*, *Tagln*, *Mef2c*, *Bmp1*, *Zfp423*, *Fabp4*, *Wnt5a*, *Frzb*, *Lif*, *Lpl*, *Pparg*, *Igf1*, *Il6st*, and *Hif1a*; lower hair follicle (main cell type identity) – by *Nfatc1*, *Sox9*, *Krt15*, *Lhx2*, *Cd34*, *Lgr5*, *Tcf3*, and *Tcf4*; hair germ cells – *Cdh3*, *Sox4*, and *Axin2*; bulge stem cells – *Cd34*, *Krtq5*, and *Lgr5*; NAECs – by ''NAEC aggregate score'' that includes *Dleu7*, *Lypd2*, *Cldn1*, *Ntng1*, *Moxd1*, *Slc16a1*, and *Krt19* (Wolbert et al., 2020); refractory telogen – based on *Dkk1*, *Dkk2*, *Dkk4*, *Serpinf1*, *Sost*, *Wif1*, *Cer1*, *Notum*, *Sfrp1*, *Sfrp2*, *Sfrp4*, *Sfrp5*, *Igfbp4*, *Draxin*, *Sostdc1*, *Frzb*, *Bmp2*, *Bmp4*, *Gdf5*, *Gdf6*, *Gdf7*, *Bmp5*, *Bmp6*, *Bmp7*, *Bmp8*, *Bmp8a*, *Bmp8b*, *Osm*, *Fgf18*, *Inhba*, *Inhbb*, *Inhbc*, and *Inhbe*; competent telogen – based on *Fst*, *Nbl1*, *Grem1*, *Grem2*, *Chrd*, *Fgf7*, *Fgf10*, *Tgfb1*, *Tgfb2*, *Tgfb3*, *Pdgfa*, *Pdgfb*, *Pdgfc*, *Pdgfd*, *Nog*, *Bmp3*, *Lefty1*, *Lefty2*, *Wnt1*, *Wnt10a*, *Wnt10b*, *Wnt16*, *Wnt2*, *Wnt2b*, *Wnt3*, *Wnt3a*, *Wnt4*, *Wnt6*, *Wnt7a*, *Wnt7b*, *Wnt8a*, *Wnt8b*, *Wnt9a*, *Wnt9b*, *Dhh*, *Ihh*, and *Shh*; and Hedhehog-active and responsive cells – based on known Hedgehog ligands and receptors as previously described in GSEA (Subramanian et al., 2005). Aggregate marker gene module scores were Log-normalized and visualized in two-dimensional feature plots.

Modeling cellular communication networks

Intra- and intercellular communication networks were modeled based on abundance of known ligand-receptor pair transcripts with CellChat (version 0.5.0) (Jin et al., 2021). To identify potential communication networks perturbed or induced in control or mutant skin cells, we sub-clustered HF epithelial and mesenchymal cells and calculated over-expressed genes in each data set, followed by significant ligand-receptor interactions using the *identifyOverExpressedGenes* and *identifyOverExpressedInteractions* functions, respectively, with default parameters. Normalized raw counts were used as input into CellChat. Pre-processing functions were performed with default parameters. We used a user-modified version of the CellChat mouse database (CellChatDB) of ligand-receptor pairs as 'ground-truth' to model communication networks. In this modified version of the mouse CellChatDB, we included *Scube3* as a putative ligand of the TGFβ signaling pathway with associated *Tgfbr1*/*Tgfbr2* receptors. This interaction was given the interaction name ID: *Scube3* – (*Tgfbr1-Tgfbr2*). We did not include any agonists or antagonists in this putative interaction. Communication probabilities were calculated with *computeCommunProb*. We filtered communications where a minimum of 10 cells per group were present and inferred communication networks at a signaling pathway level using *computeCommunProbPathway* with default parameters. The aggregated communication networks were calculated with the function *aggregateNet* with default parameters, and the relative contribution of individual ligand-receptor pairs to the aggregate communication network were visualized separately. To identify conserved and induced/perturbed communication networks in control and mutant datasets, we performed joint manifold and classification learning analyses based on functional similarities using the functions *computeNetSimilarityPairwise*, *netEmbedding* and *netClustering* with the ''functional'' argument enabled.

Modeling Gene Regulatory Networks (GRNs)

GRNs were modeled with pySCENIC (version 0.10.2) (Van de Sande et al., 2020) in a Python environment (Version 3.7). Briefly, pre-processed Seurat objects were converted to loom files. We then pre-defined a list of mouse transcription factors (TFs) (https://github.com/aertslab/pySCENIC/blob/master/resources/mm_mgi_tfs.txt) and inferred regulatory interactions between them and their putative target genes via a tree-based regression-based network inference model (GRNBoost2). Modules were then generated using the

default strategies outlined in pySCENIC. Only positively correlated modules ($\rho \geq +0.03$), which correspond to ''activating modules'', were kept for downstream query. We then performed motif enrichment and TF-regulon prediction. cisTarget motif enrichment was performed based on a ranking and recovery approach with a 10kb putative regulatory region boundary from the TSS (mm10__refseq-r80__10kb_up_and_down_tss.mc9nr.feather) (https://resources.aertslab.org/cistarget/). AUC metrics were used to assess gene recovery based on the ranking approach implemented as well as the relative biological activity of a regulon on a single-cell basis. Regulon activity was used for dimensionality reduction and visualized with two-dimensional tSNE embedding. The activity of regulons across DP/DPL cells were compared against each other and across genotypes by converting Regulon Specificity Scores (RSS) to Z-scores. The Z-scores were calculated by standardizing the average AUC scores and their standard deviation as previously described.

RNA dynamics analysis

Loom files were created using the Python script *velocyto.py* (version 0.17.17; Anaconda version 3.6-5.0.1; Python version 2.7.2) for each individual *LeprB-Cre;mTmG;SmoM2*$^{+/-}$ library. Loom files for duplicate *LeprB-Cre;mTmG;SmoM2*$^{+/-}$ libraries (i.e., replicates) were combined using loompy (version 2.0.16; Anaconda version 3.6-5.0.1; Python version 3.7.2; Spyder 4.1.5). RNA velocity was inferred with scVelo (version 0.2.2; Python version 3.7.0), which enables the recovery of full transcriptional dynamic information by leveraging splicing kinetics (Bergen et al., 2020). Briefly, a preprocessed DP/DPL object was merged with its corresponding spliced/unspliced counts. To estimate velocity, first- and second-order moments were computed, followed by velocity estimation. We implemented three distinct models of RNA velocity, including deterministic, dynamical, and dynamical with differential kinetic testing with standard parameters as suggested by developer. For visualization purposes, velocity vectors were projected as streamlines onto a two-dimensional tSNE embedding.

QUANTIFICATION AND STATISTICAL ANALYSIS

All statistical analyses were performed on at least three independent experiments, unless otherwise noted. Two-sample proportion test (alpha = 0.05) with a Bonferroni correction was performed in Python (version 2.7.2) for the analysis in Figure 4D and Unpaired Student's t-tests were performed using Prism (version 9.2.0) for the rest of the statistical analysis in this paper. All data are reported as the mean ± standard deviation (SD). Exact n value, definition of center, dispersion and precision measures were stated in relevant figure legends and text. Asterisks denote statistical significance (*$P < 0.05$, **$P < 0.01$, ***$P < 0.001$, ****$P < 0.0001$ – unpaired Student's t-test; **** $P < 0.00005$, *** $P < 0.0005$, * $P < 0.05$, n.s. – no significance – two-sample proportion test with Bonferroni correction).